REPORT DOCUMENTATION PAGE

Form Approved
OMB No. 0704-0188

The public reporting burden for this collection of information is estimated to average 1 hour per response, including the time for reviewing instructions, searching existing data sources, gathering and maintaining the data needed, and completing and reviewing the collection of information. Send comments regarding this burden estimate or any other aspect of this collection of information, including suggestions for reducing the burden, to the Department of Defense, Executive Services and Communications Directorate (0704-0188). Respondents should be aware that notwithstanding any other provision of law, no person shall be subject to any penalty for failing to comply with a collection of information if it does not display a currently valid OMB control number.
PLEASE DO NOT RETURN YOUR FORM TO THE ABOVE ORGANIZATION.

1. REPORT DATE *(DD-MM-YYYY)*	2. REPORT TYPE	3. DATES COVERED *(From - To)*
08/08/2012	FINAL	08/01/2010-07/31/2012

4. TITLE AND SUBTITLE

YIP: Understanding Nanoscale Thermal Conduction and Mechanical Strength Correlation In High Temperature Ceramics With Improved Thermal Shock Resistance For Aerospace Applications

5a. CONTRACT NUMBER

5b. GRANT NUMBER
FA9550-10-1-0426

5c. PROGRAM ELEMENT NUMBER

6. AUTHOR(S)

Dr. Vikas Tomar

5d. PROJECT NUMBER

5e. TASK NUMBER

5f. WORK UNIT NUMBER

7. PERFORMING ORGANIZATION NAME(S) AND ADDRESS(ES)
Purdue University, 701 W Stadium Ave, West Lafayette, IN-47907

8. PERFORMING ORGANIZATION REPORT NUMBER

9. SPONSORING/MONITORING AGENCY NAME(S) AND ADDRESS(ES)
Air Force Office of Scientific Research
875 N Randolph St
Arlington, VA 22203
Program Manager: Dr. Joan Fuller

10. SPONSOR/MONITOR'S ACRONYM(S)

11. SPONSOR/MONITOR'S REPORT NUMBER(S)
AFRL-OSR-VA-TR-2012-1129

12. DISTRIBUTION/AVAILABILITY STATEMENT

Distribution A: Approved for public release

13. SUPPLEMENTARY NOTES

14. ABSTRACT

This research focused on obtaining an understanding of the nanoscale physical mechanisms that govern interfacial interactions and heat transfer in materials at elevated temperatures. The underlying strategy was to understand how thermal conduction at nanoscale gets affected by factors such as the effect of quantum to molecular scale temperature related phase change, effect of nanoscale interfacial reconstruction, and effect of thermal stress affected material transformation. Issue is to enhance thermal management characteristics of materials exposed to high heating rates and high thermal gradients based on understanding gained in this research as well as to leverage this understanding to resolve thermal shock and thermal cycling affected failures in materials exposed to temperature extremes by introducing control factors related to nanoscale thermal conduction. Material systems of focus are Si based ceramics, particularly ZrB2-SiC nanocomposite interfaces. For verification purposes analyses also focus on Si-Ge interfaces and nanocomposites, as a lot of simulation data is available on this system.

15. SUBJECT TERMS

Molecular simulation, ab initio simulations, thermal conductivity, biomimetic materials, phase transformation, thermomutability, high temperature interfacial thermal measurements

16. SECURITY CLASSIFICATION OF:			17. LIMITATION OF ABSTRACT	18. NUMBER OF PAGES	19a. NAME OF RESPONSIBLE PERSON
a. REPORT	b. ABSTRACT	c. THIS PAGE			Prof. Vikas Tomar
U	U	U	U	42	**19b. TELEPHONE NUMBER** *(Include area code)* +1-765-494-3423

Reset

Standard Form 298 (Rev. 8/98)
Prescribed by ANSI Std. Z39.18

INSTRUCTIONS FOR COMPLETING SF 298

1. REPORT DATE. Full publication date, including day, month, if available. Must cite at least the year and be Year 2000 compliant, e.g. 30-06-1998; xx-06-1998; xx-xx-1998.

2. REPORT TYPE. State the type of report, such as final, technical, interim, memorandum, master's thesis, progress, quarterly, research, special, group study, etc.

3. DATES COVERED. Indicate the time during which the work was performed and the report was written, e.g., Jun 1997 - Jun 1998; 1-10 Jun 1996; May - Nov 1998; Nov 1998.

4. TITLE. Enter title and subtitle with volume number and part number, if applicable. On classified documents, enter the title classification in parentheses.

5a. CONTRACT NUMBER. Enter all contract numbers as they appear in the report, e.g. F33615-86-C-5169.

5b. GRANT NUMBER. Enter all grant numbers as they appear in the report, e.g. AFOSR-82-1234.

5c. PROGRAM ELEMENT NUMBER. Enter all program element numbers as they appear in the report, e.g. 61101A.

5d. PROJECT NUMBER. Enter all project numbers as they appear in the report, e.g. 1F665702D1257; ILIR.

5e. TASK NUMBER. Enter all task numbers as they appear in the report, e.g. 05; RF0330201; T4112.

5f. WORK UNIT NUMBER. Enter all work unit numbers as they appear in the report, e.g. 001; AFAPL30480105.

6. AUTHOR(S). Enter name(s) of person(s) responsible for writing the report, performing the research, or credited with the content of the report. The form of entry is the last name, first name, middle initial, and additional qualifiers separated by commas, e.g. Smith, Richard, J, Jr.

7. PERFORMING ORGANIZATION NAME(S) AND ADDRESS(ES). Self-explanatory.

8. PERFORMING ORGANIZATION REPORT NUMBER. Enter all unique alphanumeric report numbers assigned by the performing organization, e.g. BRL-1234; AFWL-TR-85-4017-Vol-21-PT-2.

9. SPONSORING/MONITORING AGENCY NAME(S) AND ADDRESS(ES). Enter the name and address of the organization(s) financially responsible for and monitoring the work.

10. SPONSOR/MONITOR'S ACRONYM(S). Enter, if available, e.g. BRL, ARDEC, NADC.

11. SPONSOR/MONITOR'S REPORT NUMBER(S). Enter report number as assigned by the sponsoring/ monitoring agency, if available, e.g. BRL-TR-829; -215.

12. DISTRIBUTION/AVAILABILITY STATEMENT. Use agency-mandated availability statements to indicate the public availability or distribution limitations of the report. If additional limitations/ restrictions or special markings are indicated, follow agency authorization procedures, e.g. RD/FRD, PROPIN, ITAR, etc. Include copyright information.

13. SUPPLEMENTARY NOTES. Enter information not included elsewhere such as: prepared in cooperation with; translation of; report supersedes; old edition number, etc.

14. ABSTRACT. A brief (approximately 200 words) factual summary of the most significant information.

15. SUBJECT TERMS. Key words or phrases identifying major concepts in the report.

16. SECURITY CLASSIFICATION. Enter security classification in accordance with security classification regulations, e.g. U, C, S, etc. If this form contains classified information, stamp classification level on the top and bottom of this page.

17. LIMITATION OF ABSTRACT. This block must be completed to assign a distribution limitation to the abstract. Enter UU (Unclassified Unlimited) or SAR (Same as Report). An entry in this block is necessary if the abstract is to be limited.

**YIP: UNDERSTANDING NANOSCALE THERMAL CONDUCTION AND
MECHANICAL STRENGTH CORRELATION IN HIGH TEMPERATURE CERAMICS
WITH IMPROVED THERMAL SHOCK RESISTANCE FOR AEROSPACE
APPLICATIONS**

Final Technical Report

Prepared By

Dr. Vikas Tomar
Associate Professor
School of Aeronautics and Astronautics
Purdue University, West Lafayette, IN
Email: tomar@purdue.edu Phone: (765) 494-3423

August 08, 2012

Program Manager
Dr. Joan Fuller
AFOSR/RSA
Phone: (703) 696-8457 DSN 426-8457
FAX (703) 696-7320 Email: Thermal@afosr.af.mil

Purdue University
3205 ARMS, 701 W Stadium Ave
West Lafayette, IN-47907

DISCLAIMER

This report was prepared as an account of work sponsored by an agency of the United States Government. Neither the United States Government nor any agency thereof, nor any of their employees, makes any warranty, express or implied, or assumes any legal liability or responsibility for the accuracy, completeness, or usefulness of any information, apparatus, product, or process disclosed, or represents that its use would not infringe privately owned rights. Reference herein to any specific commercial product, process, or service by trade name, trademark, manufacturer, or otherwise does not necessarily constitute or imply its endorsement, recommendation, or favoring by the United States Government or any agency thereof. The views and opinions of authors expressed herein do not necessarily state or reflect those of the United States Government or any agency thereof.

TABLE OF CONTENTS

EXECUTIVE SUMMARY

This research focused on obtaining an understanding of the nanoscale physical mechanisms that govern interfacial interactions and heat transfer in materials at elevated temperatures. The underlying strategy was to understand how thermal conduction at nanoscale gets affected by factors such as the effect of quantum to molecular scale temperature related phase change, effect of nanoscale interfacial reconstruction, and effect of thermal stress affected material transformation. Issue is to enhance thermal management characteristics of materials exposed to high heating rates and high thermal gradients based on understanding gained in this research as well as to leverage this understanding to resolve thermal shock and thermal cycling affected failures in materials exposed to temperature extremes by introducing control factors related to nanoscale thermal conduction. Material systems of focus are Si based ceramics, particularly ZrB_2-SiC nanocomposite interfaces. For verification purposes analyses also focus on Si-Ge interfaces and nanocomposites, as a lot of simulation data is available on this system.

In terms of modeling the required phenomenon, classical analytical approaches could not be used because of small length scales at material interfaces. Classical molecular dynamics or Monte Carlo methods based approach could not be used because classical interatomic potential used in such approaches are not capable of correctly describing phase transformation, high temperature property changes, and electronic properties which must be correctly described in order to properly understand such phenomenon. There have been significant advancements in experimental measurements of thermal conduction. However, such advancements have not addressed *in-situ* high temperature thermal conduction as well as thermal conduction under applied stress and/or strain. Therefore, developments were made both in terms of modeling and experiments in this research to model the required material thermal behavior. A new experimental approach was developed to perform *in-situ* measurements of temperature dependent thermal conduction behavior as a function of applied stress/strain. The experimental developments were coupled with new developments in non-equilibrium Green's function based *ab-initio* calculations of nanostructure thermal conductivity.

Using *ab-initio* modeling it was revealed that interatomic separation in semiconducting as well as high temperature materials in single crystalline state as well as in interfacial configurations is intricately linked to change in both electronic and phononic (lattice) density of states, especially at high temperatures. Such relation occurs to different extents in metal, semiconductor, and ceramic single crystals. *Ab-initio* simulations were used to highlight important role played by electronic thermal conductivity in overall thermal conduction across interfaces at high temperatures. This is the first time, quantum simulations of electronic and phononic thermal conductivity across interfaces in a realistic material interface were reported. *Ab-initio* analyses have also revealed new insights regarding role of temperature and stress in phonon, electron, and coupled phonon-electron affected heat conduction in model metal (Au), semiconductor (Si), and ceramic (SiC) materials. It was shown that electronic thermal conductivity becomes a significant part of a material's thermal conductivity at elevated temperatures. Calculations were used to understand unresolved experimental findings regarding electronic thermal conductivity issues and related failure issues in high temperature materials on experiments performed by Fahrenholtz group and Dave Marshall's group. Discussions are underway on how such analyses be used to aid directed processing of high temperature thermal shock resistant ZrB_2 based composites. The analyses are also underway to predict quantum mechanistic ways to reduce thermal shock and

thermal cycling related failure in such materials. We have also performed classical molecular simulations of thermal conduction in nanoscale microstructures in order to examine scale up of the findings of classical *ab-initio* simulations to realistic system sizes. We have proven for the first time that materials with biomimetic phase morphology have thermal conductivity values independent of strain. This finding has strong implication for developing materials with thermal properties independent of applied stress. We have proven for the first time that that tensile straining and heat flow direction can be used to develop a thermal diode material from superlattice construction. In addition, our group was the first to show that nanostructures with tunable thermal diode properties could be developed based on strain engineering. For this reason, the relevant publication was featured in the Virtual J. of Nanoscale Science and Technology (A collection of significant advances in nanotechnology).

Experimental analyses have revealed new insights regarding correlation between lattice distortion and lattice vibrations previously not possible owing to the unavailability of experiments. Now new inroads could be made into strain dependent thermal engineering based on the findings. We have also performed first ever measurements of nanoscale and microscale high temperature creep in a ceramic. Such measurements could lead to significant advances in tunable thermal protection systems operating at temperatures ranging from very low to ultra-high. We have used this system for first ever measurements of thermal conductivity change in a deforming material as a function of temperature. Now experiments at elevated temperatures up to 1000 K are underway. A request with AFoSR is pending to modify this system to be able to perform measurements at temperatures up to 2500 K. Our experiments for the first time show that thermal conductivity of even a single crystal shows significant changes with deformation and such deformation dependent thermal conductivity is strongly correlated to nanoscale stress-strain curves. Correspondingly, thermal protection/management systems may perform in a different way under stress or environmental changes in comparison to their original design. Ours is the only experimental setup able to perform such measurements at the nano and micron scale. Significant applications are in the areas of fault tolerant thermal protection systems, topological meta materials, quantum coherent sensing etc.. The progress made in this program can also be leveraged for solving unique problems such as interfacial thermal stress/thermal conduction problems at metal-non/metal interfaces (CNT-Au or similar), innovative solutions in transient heat transfer, and environment dependent heat transfer in conditions such as nuclear or high temp environments or high mach flow or corrosive environments etc. This framework can also be leveraged for unique solutions in multiphase or small scale phase transformation heat transfer which has not been possible till now because of limitations of classical molecular simulations and related experiments.

LIST OF PUBLICATIONS RESULTING FROM GRANT SUPPORT

International Journal Publications:

1. Samvedi, V. and Tomar, V. (2012a). "An ab-initio study of coupling between electronic and phononic contribution to stress dependent thermal conductivity of Au, Si, and SiC." Journal of Nanomechanics and Micromechanics. Submitted February 1, 2012; accepted March 9, 2012; posted ahead of print March 12, 2012. doi:10.1061/(ASCE)NM.2153-5477.0000046.
2. Samvedi, V. and Tomar, V. (2012b). "Ab-Initio study of softening of ZrB_2-SiC material at high temperatures and strains: Correlating phononic and electronic thermal contributions " In Review in J. European Ceramic Society.

3. Gan, M, and Tomar, V., 2011, Correlating Microscale Thermal Conductivity of Heavily-doped Silicon with Simultaneous Measurements of Stress, ASME Journal of Engineering Materials and Technology, Vol. 133, 041013 (5 pp).
4. Gan, M. and Tomar, V. (2011b). "Scale and temperature dependent creep modeling and experiments in materials." JOM Journal of the Minerals, Metals, and Materials Society **63**(9): 27-34.
5. Tomar, V., and Samvedi, V., 2010, Correlation of thermal conduction properties with mechanical deformation characteristics of a set of SiC-Si3N4 nanocomposites, Journal of Engineering Materials and Technology, Volume 133, Issue 1, 011013 (7 pages)
6. Gan, M, and Tomar, V., 2010, Role of length scale and temperature in indentation induced creep behavior of polymer derived Si-C-O ceramics, Materials Science and Engineering-A, Volume 527, Issues 29-30, Pages 7615-7623
7. Samvedi, V., and Tomar, V., 2010, Role of Straining and Morphology in Thermal Conductivity of a Set of Si-Ge Superlattices and Biomimetic Si-Ge Nanocomposites, J. Phys. D: Appl. Phys. 43 (2010) 135401 (11pp)
8. Samvedi, V, and Tomar, V., 2009, Role of interface thermal boundary resistance in overall thermal conductivity of Si-Ge multi-layered structures, Nanotechnology 20 (2009) 365701 (11pp) (Special Mention by Editors and Reviewers)
9. Samvedi, V, and Tomar, V., 2008, Role of heat flow direction, monolayer film thickness, and periodicity in controlling thermal conductivity of a Si-Ge superlattice system, *Journal of Applied Physics (featured in Virtual Journal of Nanoscale Science and Technology, volume 19, issue 4), vol 105, 013541*

Conference Publications and Presentations:
10. Samvedi, V., and Tomar, V., 2011, A quantum mechanical study of the thermal conduction across a ZrB_2-SiC interface as a function of temperature and strain, ASME Interpack 2011, July 6-8, 2011, Portland, Oregon, INTERPACK2011-52283
11. Samvedi, V., and Tomar, V., 2011, Role of interface thermal boundary resistance, straining, and morphology in thermal conductivity of a set of si-ge superlattices and biomimetic si-ge nanocomposites, ASME Interpack 2011, July 6-8, 2011, Portland, Oregon, INTERPACK2011-52284
12. Samvedi, V., and Tomar, V., 2011, A quantum mechanical study of the thermal conduction across a ZrB_2-SiC interface as a function of temperature and strain, Joint ASME-JSME International Heat Transfer Conference, March 13 - 17, 2011, Honolulu, HI, paper number AJTEC2011-44643
13. Samvedi, V., and Tomar, V., 2011, Role of interface thermal boundary resistance, straining, and morphology in thermal conductivity of a set of si-ge superlattices and biomimetic si-ge nanocomposites, Joint ASME-JSME International Heat Transfer Conference, March 13 - 17, 2011, Honolulu, HI, paper number AJTEC2011-44644
14. Samvedi, V., and Tomar, V., 2010, Controlling thermal diffusion by nanoscale structural arrangement and dopinsg in Si-Ge superlattices, 20th National and 9th International. ISHMT-ASME Heat and Mass Transfer Conference. January 4-6, 2010, Mumbai-India

STUDENTS SUPPORTED
Two students were supported on the project on 50% RA (Ming Gan and Vikas Samvedi) appointments. Students are currently in advanced stages of their PhD study. Together we have reported project findings in international journal publications highlighted above.

AWARDS AND RECOGNITIONS
The following awards and recognitions were received as a result of work performed during supported research.

- 2012-13 Bilsland Dissertation Fellowship to Student Ming Gan (Awarded to nearly 15 students annually out of approximately 1500 graduate students in Purdue University Engineering program)
- Awarded tenure and promotion to associate professor in 2011
- Elsevier-Materials Science and Engineering-C Inaugural Young Researcher Award for excellence in research at the interface of biology and materials engineering by a researcher under age 35 (2010), Based on biomimetic material research, reference 7 in journal publication list
- American Society of Mechanical Engineers (ASME) Materials Division "Orr" Family Award for excellence in failure of materials research (2010) with emphasis on thermal and mechanical coupling's role in material failure, related to refs 3, 4, 5, 6 in journal publication list
- The minerals, metals, and materials society (TMS: http://www. tms.org) Early Career Faculty Fellow-Honorable Mention (2010) based on work in this area
- Keynote and Invited Talks at Oberwolfach Workshop-Germany (Oberwolfach Fellow)-2012, International Plasticity Conference-2012, International Conference on Heterogeneous Material Mechanics-2011, TMS MS&T Meeting-2009,American Ceramic Society PACRIM Conference-2009

NARRATIVE

This research focused on obtaining an understanding of the nanoscale physical mechanisms that govern interfacial interactions and heat transfer in materials at elevated temperatures and the corresponding thermal stresses. The underlying strategy was to understand how thermal conduction at nanoscale gets affected by factors such as the effect of quantum to molecular scale temperature related phase change, effect of nanoscale interfacial reconstruction, effect of stress affected material transformation. Issue is to leverage this understanding to resolve thermal shock and thermal cycling affected failures in high temperature materials by introducing control factors at the nanoscale which are obtained based on understanding gained in this research. Material systems of focus are Si based ceramics, particularly ZrB_2-SiC nanocomposite interfaces. For verification purposes analyses also focus on Si-Ge interfaces and nanocomposites, as a lot of simulation data is available on this system.

In terms of modeling the required phenomenon, classical analytical approaches could not be used because of small length scales at material interfaces. Classical molecular dynamics or Monte Carlo methods based approach could not be used because classical interatomic potential used in such approaches are not capable of correctly describing phase transformation, high temperature property changes, and electronic properties which must be correctly described in order to properly understand such phenomenon. There have been significant advancements in experimental measurements of thermal conduction. However, such advancements have not addressed *in-situ* high temperature thermal conduction as well as thermal conduction under applied stress and/or strain. Therefore, developments were made both in terms of modeling and experiments in this research to model the required material thermal behavior. A new experimental approach was developed to perform *in-situ* measurements of temperature dependent thermal conduction behavior as a function of applied stress/strain. The experimental developments were coupled with new developments in non-equilibrium Green's function based *ab-initio* calculations of nanostructure thermal conductivity.

In the following the experimental and computational advances and the corresponding physical findings are delineated.

§1 EXPERIMENTAL DEVELOPMENTS

Experimental methods to measure thermal conductivity at microscale and nanoscale structures fall into two main categories – electrical and optical. The difference between the two types of techniques is the type of heating source used. A range of different shapes e.g. thin films [1-3], micro-cantilevers [4, 5], micro-bridges [6, 7], and suspended membranes [8-11] have been analyzed using such techniques. In the electrical techniques, metallic films deposited or machined on the silicon structures are used as a heating source by applying a current through the films [2]. Temperature of the silicon device at different locations is measured by such metallic films using electrical-resistance thermometry. In the case of optical techniques, a focused laser source is used as the heating source [4]. In contrast to electrical techniques optical ones are contact free. Therefore, the sample preparation is simpler than that in the case of other techniques. However, the difficulty in evaluating the absorbance ratio of the incident laser leads to uncertainty in the optical measurements. Both techniques, however, can not yet analyze stress/strain dependent thermal conductivity as a function in a single experiment.

A new experimental method by the PI's group has been established to analyze strain and stress dependent thermal conduction properties as a function of temperature from nanoscopic length scale to microscopic length scale. In this experimental method time resolved Raman Spectroscopy technique for performing coupled thermal and mechanical measurements in high temperature materials at small scales has been developed. Another uniqueness of the setup is the capability to analyze thermal and mechanical cycling induced failure at high temperatures. At the heart of this setup is a combination of a nanomechanical stage with Raman spectroscopy, several multispectral thermometry stages, and a resistance thermometry. The nanomechanical stage also incorporates a scanning probe microscope to visualize the change in material morphology under straining. Since the chemical structure of the material can only be visualized using electron microscope observations (which is not in the setup), quantum mechanical simulations are used to correlate scanning probe and Raman measurements of thermal conductivity and mechanical deformation. The nanomechanical stage works at a range of temperatures approaching 750 °C and has one nanoscale and one microscale head enabling high temperature and multiscale measurements. During the measurements the sample can be deformed to produce defects. In this way, the impact of defects on the thermal conductivity can be studied *in situ*. This approach is inherently different from the standard scenario where the sample needs first to be deformed and then studied for thermal conductivity afterwards. In this standard strategy, the sample may undergo significant reconstruction when it is transferred from the mechanical deformation area to the thermal measurement. Thus, only *in situ* measurements of deformed samples enable the real time measurement of the impact of defect formation effect on the thermal conductivity. This setup is uniquely poised to quantitatively evaluate interfacial stress, interfacial thermal conduction, and interfacial phase change as a function of temperature (approaching 1000 K) in a single *in-situ* setting simultaneously.
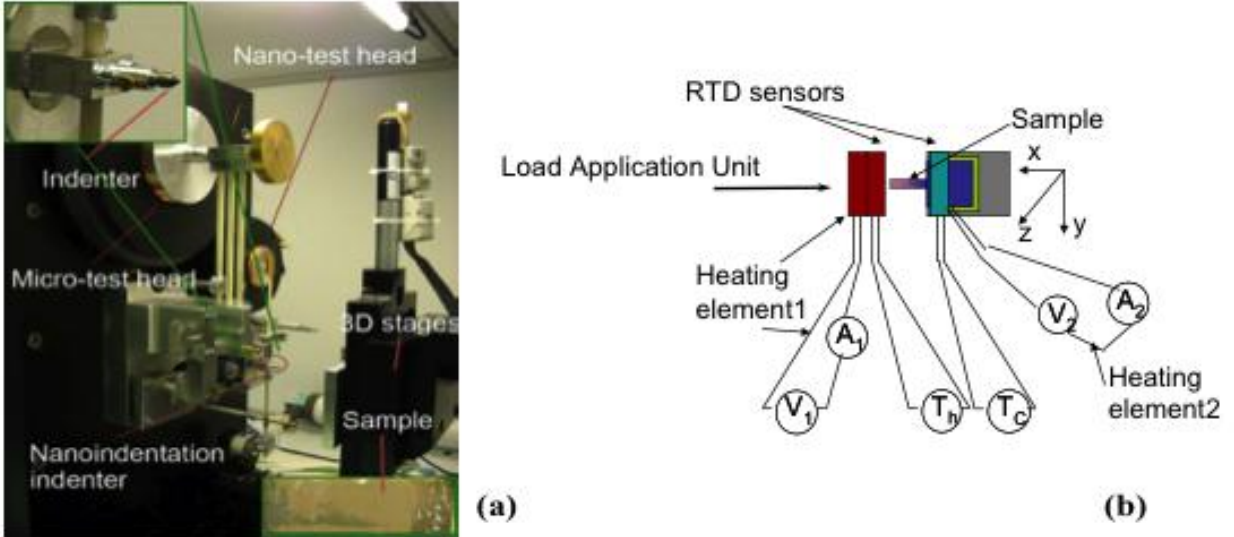
Fig. 1 (a) Experimental setup of simultaneous compressing and measuring thermal conductivity as a function of mechanical deformation and temperature and **(b)** schematic of the experimental arrangement.

The setup has been used to study high temperature nanoscale to microscale mechanical deformation in SiC based ceramics recently. This is first such advancement where high temperature measurements upto 500 degree-C were performed for the first time. Later on the setup was used to measure and report thermal properties of a microscale Si Cantilever as a function of applied stress-strain and temperature, with such variations being performed *in-situ*. In the following the experimental results are described in detail.

§1.1 MEASUREMENT OF TEMPERATURE DEPENDENT AND STRESS DEPENDENT THERMAL PROPERTIES

The setup for the measurements is shown in Fig. 1. An AFM cantilever (Aspire conical AFM tip CT170 from Nanoscience Instruments, Inc., AZ) was used as the sample. The cantilever is made up of highly doped single-crystal silicon. It has rectangular cross-section with the width of $42\,\mu m$ and the thickness of $6.5\,\mu m$. The length of the cantilever is $225\,\mu m$. The tip is located at the very end of the cantilever, where it has a triangular shape. Two different sets of samples made in two different batches were analyzed (now referred to as sample type 1 and sample type 2). Due to the micrometer size of the cantilever, the heat flow through the structure is low. Therefore, the precision of the heating power measurement and temperature measurement plays an important role in the whole experiment. In the temperature range of our measurement resistance temperature detector (RTD) is the best choice for temperature measurement. It has a tolerance of less than 0.1%, repeatability better than 0.1°C, and response time less than 2s. The standardized platinum RTD devices have accurate resistance-temperature relationship after calibration, so they are also good candidate of precise heaters. The heating module consists of two PT100 RTD devices (Minco, MN, USA). It is 1.7 mm in length, 1.3 mm in width, and 0.7 mm in thickness. In the experiment, a constant voltage was applied to the heating circuit. Both the voltage and the current (V_i and A_i in Fig. 2, i=1,2) were monitored as a function of time. The temperature at the base end of the cantilever was monitored by another RTD sensor. Both RTD sensors were connected to a RTD temperature recorder (ThermoWorks, UT, USA) with four-wire bridge connection for the best accuracy. In the experiment, the silicon cantilever was mounted on a three-dimensional linear stage with moving resolution of 0.1 μm. A resolution of 0.1 nm movement can be achieved in the longitudinal direction with a piezo-driven nano-positioner.

As the length is the dominating dimension of the cantilever, it is assumed that the heat conduction in the longitudinal direction dominates the overall heat flow from the high temperature end (T_h) to the cold one (T_c), if temperature gradient (T_h-T_c/Length) is maintained constant. The relation between temperature gradient and one dimensional steady state heat flow is described as,

$$q = -kA\frac{dT}{dx}. \tag{1}$$

Here, q is the heat flow rate in the cantilever; k is the thermal conductivity; A is the cross-sectional area, and dT/dx is the temperature gradient in the longitudinal direction. The heat flow rate q is measured as an average of the total heat Q flown in a specific period. The cross-section A is calculated from the SEM images of cantilever. $dT(t)/dx$ is derived from the two RTD

sensors. The total energy flow Q is equal to the difference between the total input energy, Q_{in}, and the energy dissipated to the surroundings, Q_{dis}, in this time period:

$$Q = Q_{in} - Q_{dis} \tag{2}$$

The input energy Q_{in} is calculated by taking the integral of heating power to time (Eqn. 3).

$$Q_{in} = \int_{t_i}^{t_o} I^2(t) R(t) dt \tag{3}$$

The current $I(t)$ flowing through the heater was monitored during the experiment. The resistance of the heater $R(t)$ is derived from its resistance-temperature relationship, while its temperature was read from the RTD sensor attached to it.

The energy dissipation, Q_{dis}, can occur through lateral conduction or through convection. Because of relatively low measurement temperature, radiation heat loss is neglected. Because cantilever length is significantly higher than its cross sectional dimensions, lateral conduction losses through cantilever were also neglected. Dissipated energy measurements by convection and through conduction in surrounding support structures were performed during each measurement of thermal conductivity. Before each experiment, the same voltage as intended for thermal conductivity measurements was applied to the heater at zero load and temperature fluctuation was observed until equilibrium was attained. Once equilibrium is attained, due to steady state, the dissipated energy through convection is equal to the input energy. It is assumed that the energy dissipation rate remains constant during the thermal conductivity measurements that follow convective energy dissipation measurements. This reasoning is based on the fact that during dissipated energy measurements cantilever is kept $2\,\mu m$ away from the heater and during following measurements it is in contact with the heater. The temperature change of the surroundings, the heater and the cantilever during the two different types of measurements is negligible (<0.5 °C). Therefore, its effect on the energy dissipation rate can be safely assumed to be negligible.
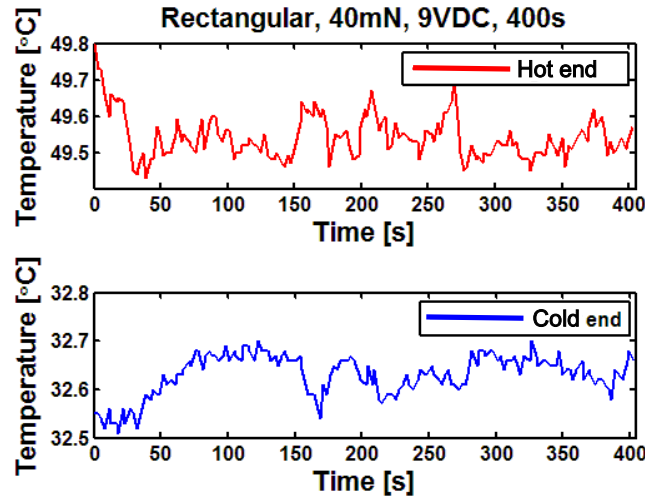
Fig. 2 Temperature profile of the hot end (T_h) and cold end (T_c). For the measurements shown a constant load of 40 mN was applied. The load was held constant for 400 s. The voltage of the heating power is 9 V DC.

Typical temperature profiles of the hot and cold ends are shown in Fig. 2. Temperature profiles fluctuate within a small range (<0.3°C). This fluctuation is within 1-2 % of the measured mean value, an acceptable error bound in all experiments in the area of reported experiments. The temperature drop from the hot end to the cold end is 17 °C. The compressive displacement of the cantilever is derived from the loading curve (Fig. 4). Generally, the initial part of the loading curve has a 'flat region', which is caused by surface roughness of the hot end heater. In the analysis, this 'flat region' was removed by taking linear fitting of the loading curve.
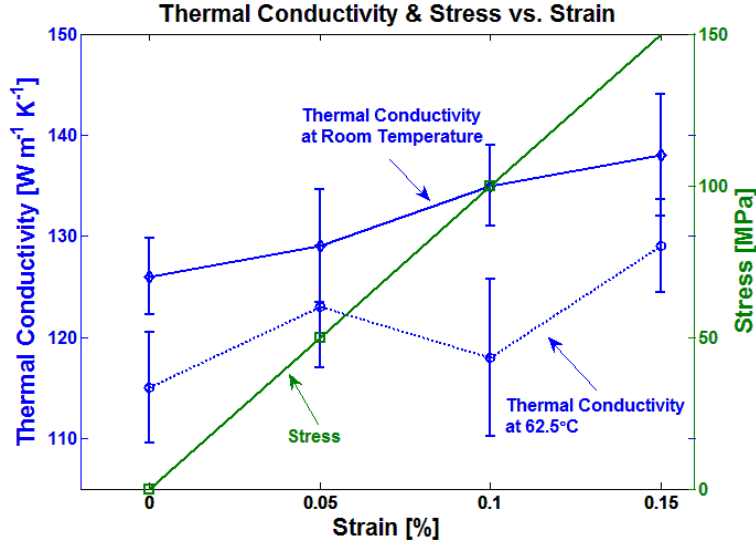
Fig. 3. Thermal conductivity as a function of strain, stress, and temperature level with such variations being performed *in-situ*

The calculated thermal conductivity as a function of applied strain and temperature is shown in Fig. 3. As shown, the thermal conductivity shows an increase as the compressive strain level increases and decrease with increase in temperature. This trend of the thermal conductivity matches simulation results reported in literature, [13], for zero percent strain. The temperature dependence data and stress dependence data is being reported in this research for the first time. The thermal conductivity variation is as large as 20 % to 40 % depending upon the applied strain. The corresponding stress percentage change is almost the same as the thermal conductivity percentage change. This finding indicates that both thermal conductivity and stress in a sample can vary in the similar manner as a function of applied strain. This is particularly important for small scale devices which operate at high number densities and at high thermal stress levels. Thermal management analyses of such devices based on 0% strain thermal conductivity values may give incorrect prediction of thermal stress.

The thermal conductivity measurements at elevated temperatures approaching 1000 K are in progress. Such setup combines the results just described with author's work on high temperature nanoscopic and microscopic mechanical property measurements which were partially supported by this project funding. The next section describes and discusses findings in those measurements.

§1.2 MEASUREMENT OF HIGH TEMPERATURE PROPERTIES

Nanoindentation creep has been observed in a wide range of materials including glasses, ceramics, and metallic materials, [12-14]. The indentation creep rate for high melting point

materials can be of the order of 5×10^{-5} s^{-1}. This is a large value when compared to the corresponding bulk strain rate. The models for indentation creep are the same as those for bulk creep, with the equivalent stress exponent, n, used as an indicator of the creep mechanism,[12]. It is believed that when the value of n is 1, creep is controlled by vacancy diffusion as deformation mechanism, [15, 16]; when the n value is 2, the creep mechanism the controlled by grain boundary sliding, [17]; when n is 3, diffusion-controlled dislocation motion dominates as deformation mechanism, [18, 19]; and when n is 5, it is dislocation climb-controlled creep mechanism, [20]. During indentation creep tests on certain metals, alloys, and ceramics at room temperature, high n values up to hundreds have been observed, [14, 21-26]. The mechanism behind such high stress exponent values has been attributed to volumetric densification and dislocation pile up. Materials systems analyzed include metallic thin films, e.g. Cu, Al, Ni, [27-29], thin films made of metallic alloys, e.g. Ni$_3$Al, [30], and ceramics e.g. ZrO2, [31], and SiC-based, [32-34]. During such studies, the size of the indenter (owing to indentation size effect-ISE) and the grain size of the polycrystalline materials have been shown to strongly affect the indentation creep response of materials. Besides the indentation size effect (ISE) and the grain size effect, the creep deformation mechanism is also shown to be affected by the test temperatures and the change in microstructure of the material as a result of temperature change. It has also been shown that fiber reinforcement, [35], or particle reinforcement, [36], can constrain creep rate. This work for the first time presented nanoindentation and microindentation creep analyses on polymer derived Si-C-O ceramic coatings at temperatures ranging from room temperature to 500 degree-C.
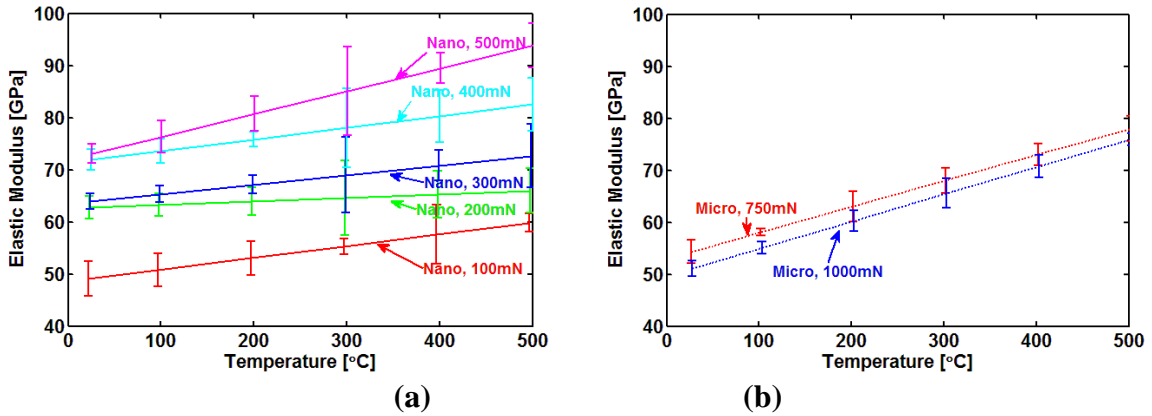
Fig. 4: **(a)** Nanoindentation elastic moduli and **(b)** microindentation elastic moduli of Si-C-O coatings as a function of temperature and maximum indentation load

Fig. 4 shows the elastic moduli values as a function of testing temperature and peak indentation load. As shown, the elastic moduli increase with increase in temperature and with increase in peak load at the nanoscale. At the microscale the elastic moduli increase as a function of temperature. However, dependence on the peak load at the microscale is not clear. Increase as a function of peak load signifies the ISE. It has been shown that Young's modulus of SiO$_2$ will increase with temperature due to compaction and distortion of SiO4 tetrahedra in the temperature range of experiments. The underlying SiCO matrix retains this attribute. An examination of Fig. 4 (a) reveals the ISE is stronger at higher temperatures. The ISE is absent in the case of microscale data. The reason behind the observation of ISE at the nanoscale is not clear. For each

data point in Fig. 4 (a), a minimum of 16 tests were performed. Therefore a possibility that a single microstructural aberration is contributing to the ISE is ruled out. At the nanoscale the nanoindenter radius is approximately 20 nm and projected area is approximately 0.5 μm^2. Accordingly, the indenter samples either the SiC particles or small spaces of SiCO matrix between adjacent $TiSi_2$ particles. The ISE, therefore, can be attributed to increasing nanoscale densification with increasing indentation depth. At the microscale collective deformation of a sample volume containing many SiC particles takes place. Due to such collective motion of particles under indenter tip, the effect of volumetric densification under indenter tip is minimzed leading to the absence of ISE. Increase in temperature contributes to increased binding of $TiSi_2$-SiCO interfaces invariably leading to increase in the elastic moduli values as a function of temperature at both scales.
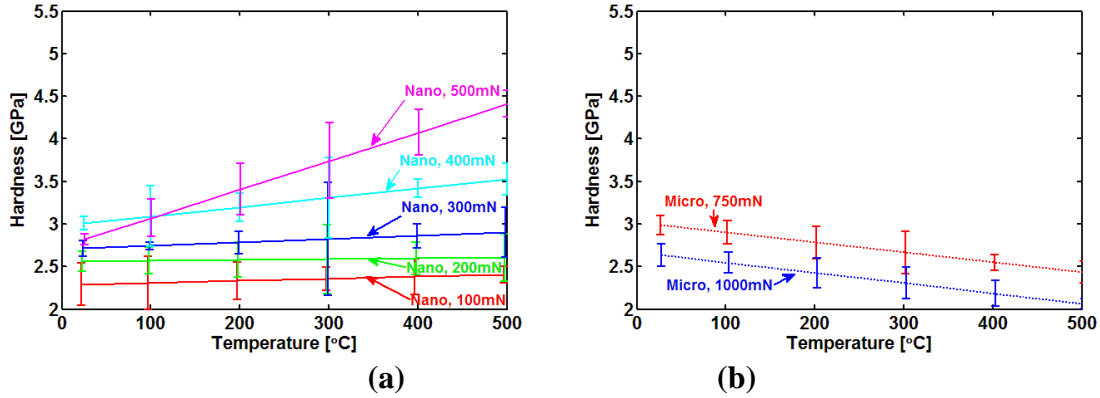

Fig. 5: **(a)** Nanoindentation hardness and **(b)** microindentation hardness of Si-C-O coatings as a function of temperature and maximum indentation load

Figure 5 plots the hardness data corresponding to the moduli plots in Fig. 5. As shown, at the nanoscale the trend for the elastic moduli is repeated for the hardness values. A clear trend on increase in Meyer's exponent with increase in temperature emerges from nanoindentation data. The microindentation hardness data trend is opposite to the trend shown in the case of microindentation elastic moduli. Hardness decreases as the measurement temperature increases. In addition, hardness reduces with increase in the peak indentation load, signifying strain softening of the material. Reduction of hardness with increase in temperature is attributable to stronger $TiSi_2$ particles pressing in relatively softer SiCO\matrix getting progressively softer with increase in temperature at the microscale. At the nanoscale not enough contact area is available to have such an effect. Data on correlation between temperature dependent hardness and young's moduli values for ceramics is not available in the literature. A similar trend (increase in moduli and decrease in hardness as a function of temperature) has been observed for Chromium steels by Medved and Bryukhanov [37].

It has been shown that in Si-C-O PDCs in amorphous phase the deformation during indentation occurs due to volumetric densification events. It has been shown that volumetric densification promotes strain hardening in vitreous silica under both indentation and diamond-anvil compression experiments, [34]. The microindentation experiments on the present materials in the amorphous state reveal a reduction of indentation hardness under increasing applied loads, indicating densification-assisted strain softening of these materials, [34]. A combination of

nanoscale and microscale results points that individually neither the SiCO matrix nor TiSi$_2$ particles show strain softening. However, mechanistic effects related to their combined presence at the microscale results in strain softening behavior. Cheng and Cheng, [38], have pointed out that indentation hardness is not a function of indentation depth for materials that truly follow power-law strain hardening. This is in contrast to the nanoindentation and microindentation results from the present materials that show an increase in hardness with increasing load during nanoindentation and reduction in hardness with increasing load during microindentation. Apart from the influence of strain hardening or softening, material pile-up around the indent and indentation creep can also contribute to indentation hardness behavior observed in the present work.
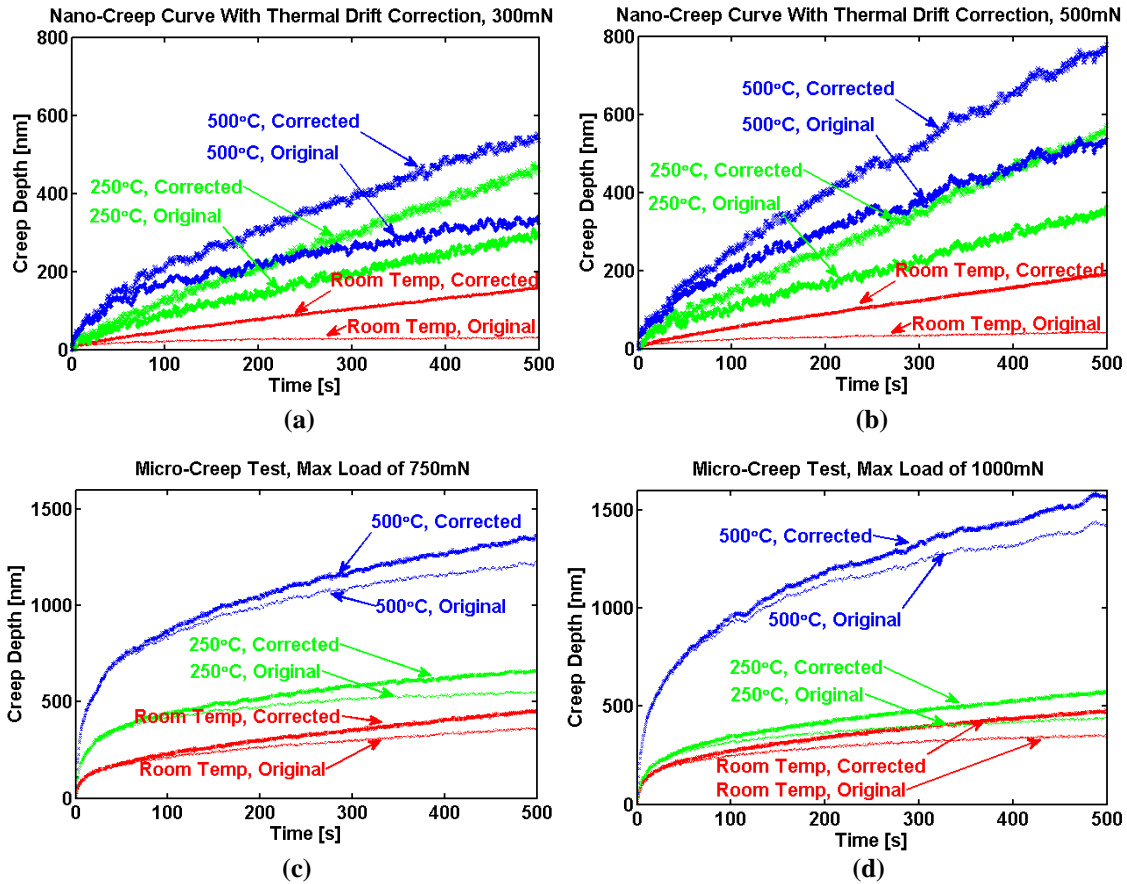
Fig. 6: Indentation depth (original and thermal drift corrected) as a function of time at different temperatures in the case of **(a)** nanoindentation test at the peak load of 300 mN, **(b)** nanoindentation test at the peak load of 500 mN, **(c)** microindentation test at the peak load of 750 mN, and **(d)** microindentation test at the peak load of 1000 mN

Figure 6 plots creep depth as a function of dwell period at three different temperatures at two different nanoindentation and microindentation peak loads. Creep data is normalized by subtracting the initial depth of each creep test. For comparison, the plots also show the thermal drift uncorrected as well as corrected data. As expected, the effect of thermal drift correction is the highest at the highest temperature and at the nanoscale. The creep depth vs. time plots

reached steady state within first 100 s of plotting in all cases. Effect of temperature is to increase the creep rate. The temperature effect is more pronounced at the micro scale in comparison to the nanoscale. The trend is particularly strong when transitioning from 250 ^{o}C to 500 ^{o}C.
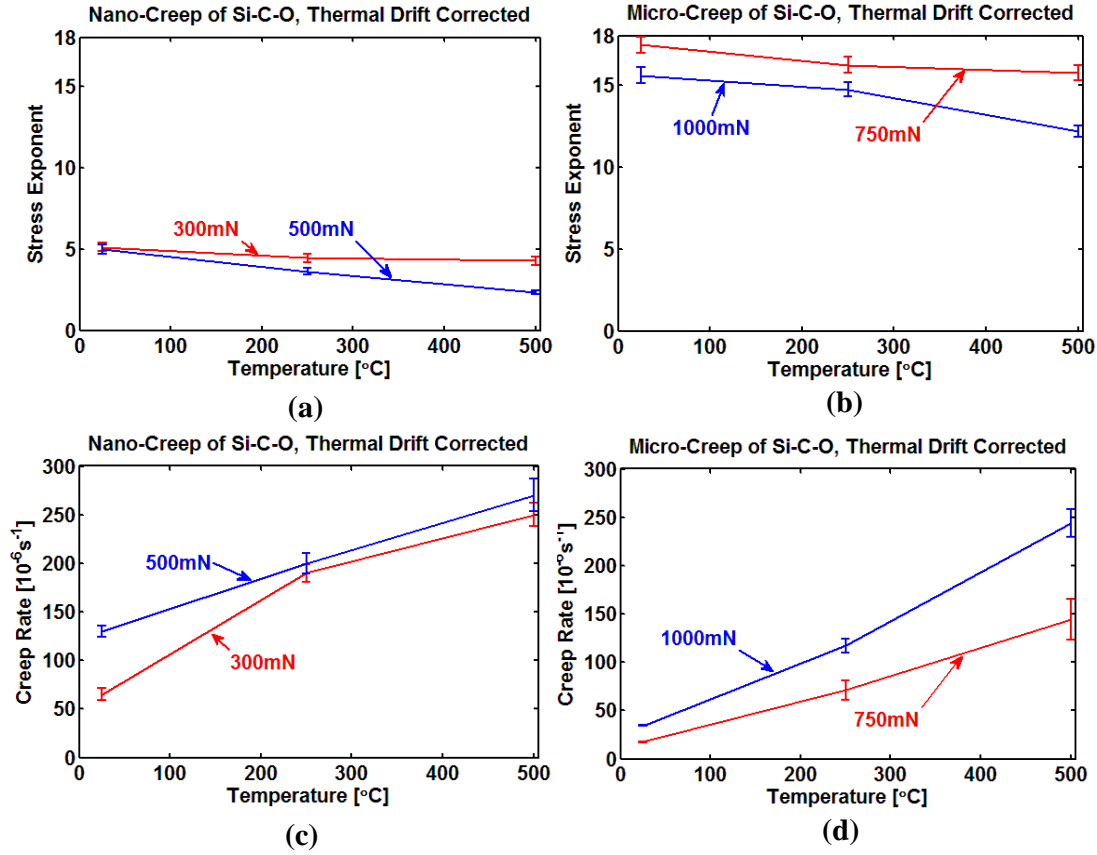
Fig. 7: (a) stress exponent as a function of load during nanoindentation creep measurements, **(b)** stress exponent as a function of load during microindentation creep measurements, **(c)** creep strain rate as a function of load during nanoindentation creep measurements and **(d)** creep strain rate as a function of load during microindentation creep measurements

Figure 7 plots stress exponent and creep strain rate as a function of temperature and peak indentation load at both length scales. Stress exponent at the nanoscale lies in the range of 4 to 5 indicating a dislocation climb related creep deformation mechanism occurring through bulk or pipeline diffusion of dislocations. The exponent reduces with increase in temperature indicating a transition of mechanism from dislocation climb to diffusion. The densely dislocated structure with high dislocation density under indenter may result in dense dislocation channels directing atoms from dislocated cores to free surfaces resulting in such a mechanism occurring at low homologous temperatures. At the microscale the stress exponent is considerably higher indicating that primary mechanism of deformation is volumetric densification. Such a transition suggests a rapid change of mechanism from linear diffusion flow to power law mechanism (e.g. climb) and eventually to rate insensitive plastic flow (dislocation glide) as the indentation size moves towards microscale regime. The disparity in stress exponent values at the two length scales is not reflected in the creep strain rate data. As shown, the creep strain rates at both length

scales lie in the same range with microscale data being on the lower side. Creep strain rate generally increases as a function of increase in temperature as well as with increase in peak indentation load. The creep strain rate at the microscale being lower than that at the nanoscale can be attributed to the averaging effect of measurements. As discussed earlier, in the case of microscale measurements, the indenter covers an area that is approximately 10 times larger than the nanoindenter area. Since hardness reduces and creep strain rate increases with increase in temperature at the microscale, the strain rate sensitivity index (constant k in relation $\sigma = b \dot{\varepsilon}^{k}$) indicates strain softening at the microscale. The same analyses reveal strain hardening at the nanoscale.

(a) **(b)**
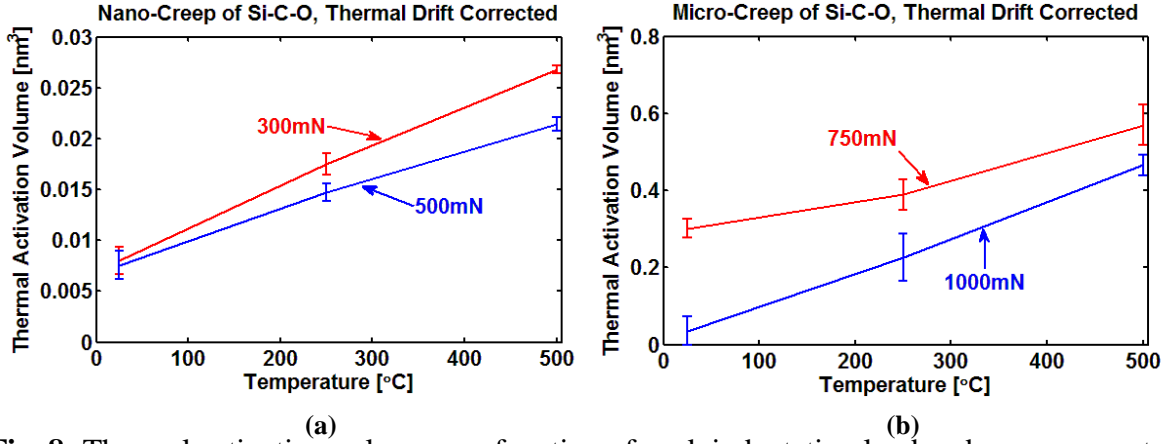
Fig. 8: Thermal activation volume as a function of peak indentation load and measurement temperature at **(a)** nanoscale and **(b)** microscale.

In general, in the case of PDCs both dislocation dominated and volumetric densifying type of deformation mechanisms with varying degree are present during indentation. In the case of quartz, the size effect on the stress exponent can be explained by a reduction of the localized shear volume as the indent size decreases. However, in the present work the size effect is related to shift from dislocation climb and diffusion related mechanism at the nanoscale to volumetric densification at the microscale (Fig. 8). The extent of a particular type of mechanism determining deformation is governed by the availability of excess free volume which is related to thermal activation volume, which is also the average change in volume of the flow unit. Low-temperature creep deformation strain rate, $\dot{\varepsilon}$, of materials can be expressed by Arrhenius-type flow function, [39],

$$\dot{e} = \dot{e}_{o} \exp\left[-\frac{\mathrm{D}G(s)}{k_{B}T} \right].$$
(4)

In the above Eqn., $\dot{\varepsilon}_{o}$ is reference strain rate that varies with the type of material, stress level, and microstructure, $\mathrm{\Delta}G$ is the activation energy for creep or other rate-dependent process, k_{B} is Boltzmann's constant and T is temperature in Kelvin. Parameter $\dot{\varepsilon}_{o}$ is proportional to the concentration of elementary defects which cause plastic strain, [40]. The sensitivity of strain rate to stress is mainly determined by the $\mathrm{\Delta}G$ term. The thermal activation volume ($v*$) is expressed by the partial derivative of $\mathrm{\Delta}G$ with respect to stress σ, [41]. In the present work, $v*$ is approximated as

$$V^* \equiv k_B T \left. \frac{\partial \ln \dot{\varepsilon}}{\partial \sigma} \right|_{\varepsilon, T} . \tag{5}$$

The derivatives are taken at fixed strain at each temperature to constrain the influence of structure change due to work hardening and softening. Figure 10 plots the thermal activation volume calculated in this case as a function of temperature, peak indentation load, and length scale. As shown, thermal activation volume increases with increase in the length scale of measurements. Since, the thermal activation volume is directly correlated to the deformation energy, the trend implies a significantly high deformation work required at the microscale in comparison to the nanoscale. An almost linear increase in activation volume with increase in temperature implies that deformation mechanism is primarily controlled by dislocations. At the nanoscale the thermal activation volume is 10 times less than that at the microscale indicating that the dislocation pile up is restricted as well as that dislocation climb and diffusion is the main deformation mechanism. At microscale significantly higher thermal activation volume indicates availability of excess free volume in the material structure that can be eliminated by densification. A combination of earlier findings with this result indicates that with increase in length scale the deformation mechanism switches from dislocation diffusion to dislocation pileup. With increase in length scale, dislocation motion does not face significant obstacles or phase transformation related factors. Such factors, if present, will change the almost linear trend observed in Fig. 10. The observed trend of the data on peak indentation load as well as stress exponent values at room temperature are in close agreement with the work of Li and Ngan [14]. However, stress exponents are lower than those reported by Li and Ngan for fused silica, indicating a difference in deformation mechanism. The deformation mechanism is intricately linked with the microstructure of this material. The material has $TiSi_2$ particles with higher melting point embedded in SiCO matrix with lower melting point. With increase in temperature, softening of the matrix, particle sliding, and particle rearrangement contribute to deformation mechanism. The effect of these factors is more pronounced at microscale due to higher surface area sampled.

§2 COMPUTATIONAL DEVELOPMENTS

Computational advances focused on establishing an *ab-initio* approach to predict chemical composition and microstructure dependent thermal conductivity of examined materials with an account of nanoscale features. As pointed out earlier, classical molecular simulations are limited in their applicability to predict thermal properties of materials at high temperatures under rapid transient heating due to transient microstructure and chemical evolution occurring during such imposed conditions. Classical molecular simulations are also limited only to analyzing thermal transport in phonon dominated systems. A widely studied semiconductor such as Si becomes conductor at high temperatures (ban-gap reduces as a function of temperature increase) severely limiting classical molecular simulation approach's applicability to analyze small scale heat transfer even in such a material. In this research, a new quantum mechanical method based on extension of non-equilibrium Green's function method is established that could be used to study fundamental issues affecting phase change heat transfer at quantum and molecular scales. Particular application relevant to project is being able to resolve issues regarding grain boundary and interface composition and how phase change and stresses at high temperature affect thermal properties that lead to thermal shock failure. This method is used to study interfacial heat transfer in ZrB_2-SiC material system of interest to AFoSR. Since *ab-initio* approach is limited to small

system sizes because of significant computational demand, such simulations are being coupled to approximate classical molecular simulations to scale up the simulation predictions to realistic microstructure size. Accordingly, the development of *ab-initio* approach was performed together with analyses of interfacial heat transfer as a function of molecular scale morphology. Analyses have proven for the first time that materials with biomimetic phase morphology have thermal conductivity values independent of strain. This finding has strong implication for developing materials with thermal properties independent of applied stress. We have proven for the first time that that tensile straining and heat flow direction can be used to develop a thermal diode material from superlattice construction. In addition, our group was the first to show that nanostructures with tunable thermal properties could be developed based on strain engineering. For this reason, the relevant publication was featured in the Virtual J. of Nanoscale Science and Technology (A collection of significant advances in nanotechnology). In the following both, the *ab-initio* calculations and the classical molecular simulations are briefly presented.

§2.1 NON-EQUILIBRIUM GREEN'S FUNCTION BASED FORMALISM TO STUDY INTERFACIAL HEAT TRANSFER AT HIGH TEMPERATURES AND/OR UNDER TRANSIENT HEAT LOAD CONDITIONS

Though thermal conductance of a material depends both on phonons and electrons, significant percentage of past research has primarily addressed the phononic contributions. With change in temperature the ratio of phonon thermal conductance to electron thermal conductance changes. It has been argued in ceramics community that under transient heat loads such as those during thermal shock loading, electron thermal conductance can play an important role in a material's response. Therefore, understanding phonon and electron contributions to a material's thermal response, especially at high temperatures, is an important issue.

Phononic contribution to the thermal conductance has been traditionally analyzed using modeling approaches based on the Boltzmann Transport Equation (BTE). In the instances where an interface is being analyzed, variants of either acoustic mismatch model (AMM) or of diffusive mismatch model (DMM) are employed for the description of conductive heat transport. The AMM makes the assumption of thermal equilibrium achieved immediately on either side of a single abrupt junction. Calculations of the AMM only consider the materials on either side of the interfacial bond and not the interfacial bond itself. The bond at the atomic interface, however, has been experimentally shown to drive interfacial transport and scattering, [42]. DMM approach too has been shown to be limited in effectively capturing the conductive heat transport across the interfacial zone. There is no clear recipe on how to combine individual impedances for an extended channel region driven into non-equilibrium by two separate thermal reservoirs, as is commonly invoked for electron flow. Both methods ignore evolution of nanostructure at interfaces as a function of temperature or applied strain due mainly to limitation of classical interatomic potentials in ability to capture complex phase changes that may be occurring at interfaces, especially at high temperatures. Both methods also cannot account for electron thermal conductance. Electron flow has usually been formulated as a two-junction problem, making a clear conceptual separation between "contacts" that are held at separate thermal equilibrium by a battery, aided by inelastic thermalizing scattering events in them, and a "channel" or "device" region where the actual transport dynamics occurs. The viewpoint leads naturally to the non equilibrium Green's function (NEGF) technique. The NEGF formalism

calculates wave (electron or phonon) transport across the channel, and therefore takes into account masses and forces bond strengths on either side of the channel atom.

The phononic thermal conductance calculation in the present work is based on the phonon density of states and the frequency calculations. Electronic part of thermal conductance is calculated using a recent modification to the quantum mechanical NEGF method, [43]. The NEGF approach had its origins in the development of the theory of quantum electrodynamics in the late 1940's and early 1950's, and inherits this field's emphasis on perturbation expansions described in diagrammatic form. The NEGF theory was formulated by Kadanoff et al [44] and Keldysh [45]. It was later elaborated by Langreth [46] as described in the text by Mahan [47]. The problems and promise of applying this approach to electron devices has been discussed by Huag et al. [48]. NEGF approach has been extensively used to study electronic transport in nanostructures in the electronics domain, [49] and [48]. The analyses regarding the role of electrons and how their behavior changes temperature dependent properties have been limited to a certain class of material systems due to extremely high computational demands of NEGF method. A change was brought by Wang et al. [50] who applied conventional electronics-focused approach to calculate electronic thermal conductance of single chain semiconductor atoms. They proposed significant modifications in the Feynman Diagrams to simplify it to be applicable to systems with high number of electrons. An alternate approach is based on atomistic Green's function calculation by Zhang et al. [51]. However, in this approach one uses classical interatomic potentials and therefore cannot account for either complex atomistic nanostructure evolution at an interface under complex tri-axial stress states, especially at high temperatures or electron mediated as well as electron-phonon coupling mediated conductive thermal transport. Advancement is needed to address these issues so that conductive heat transport in realistic conditions in a material interface can be examined. Wang et al. [52], generalized the NEGF approach by replacing fermions with bosons as basic entities. However, such analyses have been limited to 1-D atomic chains due to the computational demand and extreme complexity of the method. The applicability of modified NEGF to boson based analysis was further utilized by various groups such as pointed out in refs [53], [54], and [55]. But this too has been limited to 1-D atomic chains due to the computational demand and extreme complexity of the method.

In this work, NEGF is modified to make it applicable to bigger atomistic systems wherever one could to strike a balance between accuracy of the calculations and reduction in the complexity and computational demand, [43]. This approach provides us with the capability to separate out the phononic and electronic contribution to the overall thermal conductance. One significant aspect of the current work is that the whole framework is based on first principles calculations and does not use a classical interatomic potential like those used in atomistic Green's function formulations. The use of first principles framework enables applicability of current work in complex nanoscale material situations such as phase change, high temperature behavior etc. The need for any interatomic potential functions has been removed by calculating the parameters based on purely electronic and phononic eigen function analysis. Such use enable addressing complex atomic structures that may also involve phase transformation.

The NEGF approach for phonon transport is implemented in two steps: first the phonon propagation equations for the contacts are partitioned out to create an equivalent open-boundary version of Newton's law for lattice vibrations in the channel. The contact states enter their

boundary condition through carefully computed self-energy matrices. Next, a thermal equilibrium condition is imposed on the contact state bilinear variables in order to compute the NEGF thermal current. The NEGF method has as its main ingredient in the Green's function, which is a function of space-time coordinates. From knowledge of this function one can calculate time-dependent expectation values such as currents and densities, electron addition and removal energies and the total energy of the system. NEGF can be applied to both extended and finite systems. To describe many-electron systems in general time-dependent external fields NEGF approach here restricts itself to a non-relativistic description based on the time-dependent Schrödinger equation (TDSE). We are utilizing this simplified NEGF approach based on first principles. The thermal conductance of the material system can be calculated by the expression provided by Wang et al. [52] also known as Taylor expansion of the Landauer Formula for thermal conductance,

$$\lambda_{[NEGF]} = 1/2\pi \int_0^\infty \omega\, t_{NEGF}\, \frac{\partial f(\omega)}{\partial T}\, d\omega, \tag{6}$$

where, the transmission function is given by

$$t_{NEGF} = \frac{1}{2} Trace \left[G^r \left(\Gamma_L + \frac{1}{2}\Gamma_n - S \right) G^a \Gamma_R \right] + \frac{1}{2} Trace \left[G^a \Gamma_L G^r \left(\Gamma_R + \frac{1}{2}\Gamma_n + S \right) \right]. \tag{7}$$

Here, G^r is the retarded Green's Function while G^a is the advanced Green's Function. Γ_L and Γ_n represent the linear and non-linear part of the frequency broadening terms, and S represents the interaction term. $\frac{\partial f(\omega)}{\partial T}$ is the probability distribution function given by Bose-Einstein Distribution ($f = 1 \left/ \left(e^{\frac{\hbar\omega - \mu}{k_b T}} - 1 \right) \right.$) in the case of phononic contribution and Fermi-Dirac distribution ($f = 1 \left/ \left(e^{\frac{\hbar\omega - \mu}{k_b T}} + 1 \right) \right.$) in the case of electronic contribution. Note that although the ingredients in this equation are calculated using open boundary Newton's law, the conductance equation itself is quantum mechanical, as it apportions a fixed phase space for each thermal mode.

For analyzing interfacial heat transfer SiC[111]-ZrB$_2$[0001] was chosen as the model system. This interface was studied along with single crystalline SiC and ZrB$_2$ systems. The interface is shown in Fig. 9. Since substantial temperature and strain related simulations along with significant post processing calculations need to be performed, only one interface is analyzed due to computational time constraints (simulations reported took 1 and a half years). All supercells have periodic boundary conditions imposed in all directions. Interfacial supercell contains sufficient vacuum space above and below the atomic slabs to minimize coupling between their free surfaces. Because of the large lattice mismatch between ZrB$_2$ (d_{ZrB2} =3.169 Å) and SiC

($d_{SiC[111]}$ =3.082 Å) we follow approach of Trivedi et al. [56] and adopt cell dimensions which impose a tensile strain on SiC to accommodate the stiffer and considerably thicker (bulk-like) ZrB_2 template. We further assume that the large strain differential associated with this coherent interface approximation does not alter the energetics of the interfacial bonding.
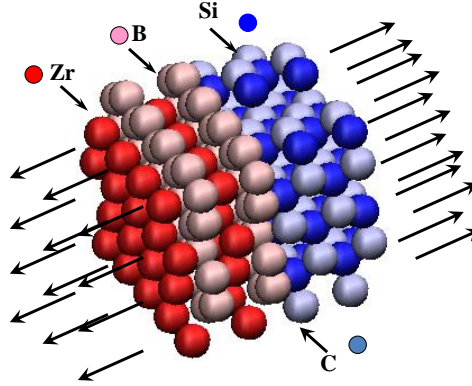
Fig. 9 The interface examined in the present research. The single crystal samples have the same overall size and orientation with respect to stretching direction depicted using arrows.

Structure calculations of the SiC [111]-ZrB_2 [0001] heterojunction were carried out using the NWChem simulation package, [57]. This program employs pseudopotentials derived from the plane-wave formalism and the Perdew91 form of the GGA functional. We used standard norm-conserving Trouiller-Martin's and Hamann pseudopotentials. A plane wave cutoff energy of 400 eV was used in conjunction with a real space grid of 16x16x16 to achieve a force accuracy of 0.01 eV/Å. This grid size was chosen after studying different grid sizes for force convergence. The atomic coordinates were fully relaxed to their zero force positions, yielding optimized atomic structures.
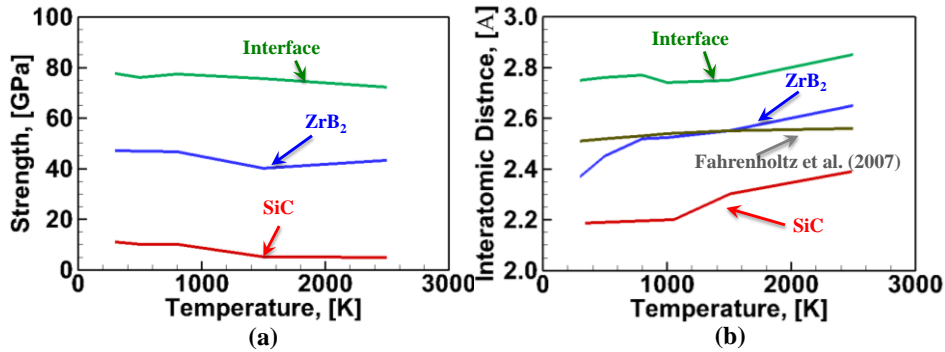

Fig. 10 (a) Tensile peak strength of single crystal ZrB_2, single crystal SiC, and ZrB2-SiC interface as a function of temperature and **(b)** average interatomic distance in single crystal SiC, ZrB_2, and SiC-ZrB_2 interface as a function of temperature. This plot also shows experimental measurement of average SiC interatomic distance reported by Fahrenholtz et al. (2007) as a function of temperature. This is the only such measurement available.

Figure 10-(a) shows peak strength as a function of temperature for the examined SiC and ZrB_2 single crystals and the SiC-ZrB_2 interface. The strength is calculated as the peak value of stress as all the examined supercells are stretched. The interface is stretched in direction shown

using arrows in Fig. 9 earlier. As shown the strength of all samples reduces with increase in temperature. Strength of interface is higher than that of ZrB_2 and SiC single crystals, as expected. It is important to note here that in the examined structures structural changes were observed as a function of strain that include bond rotation and possibly defect formation. Due to complex crystal structure it is not possible to explicitly characterize the type of defects formed (screw vs. edge dislocation, the extent of individual bond rotations due to a large number of bond angle permutations involved etc.). One way to characterize strength loss in the samples as a function of temperature is to compare average bond length of the samples as a function of temperature. Figure 10-(b) shows average bond length in the systems examined as a function of temperature. As shown in Fig. 10-(b) average bond length increase in all three samples can be correlated to the loss of strength as a function of temperature. Change in average bond length as a function of temperature also showed a similar trend (not shown). However, the change is a very small fraction (2-5%) of the average bond length values shown indicating that straining has significant bond rotations involved. Overall, however, it is interesting to note that average bond length value correlated proportionally to the loss of strength as a function of temperature. The average bond length change data as a function of temperature change is not available in literature. However, Fahrenholtz et al. [58] recently have examined average bond length as a function of temperature in SiC phase of the ZrB_2-SiC composites prepared in their lab. The trend for SiC matches with that reported by Fahrenholtz et al. [58]. It is important to note that SiC data, here, is for the single crystal and Ref [58] data is for SiC phase in a composite.
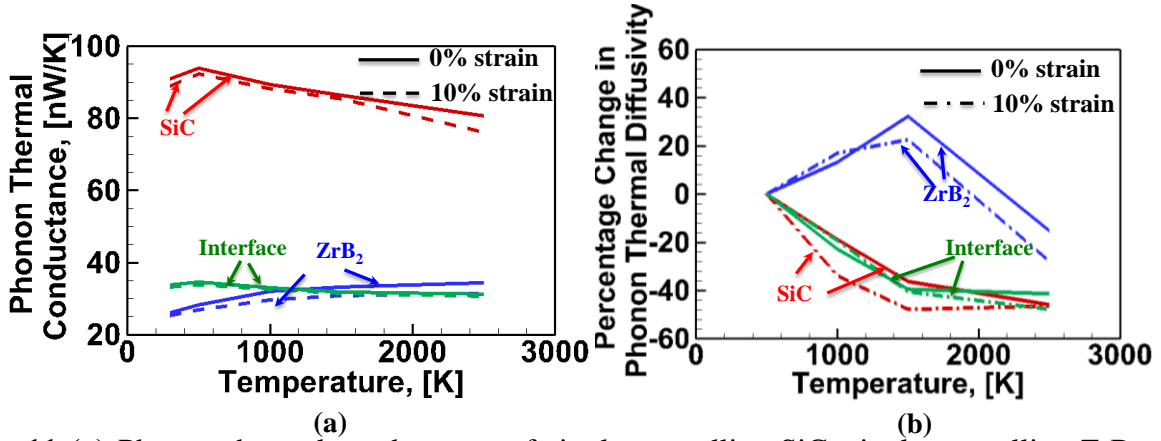
Fig. 11 (a) Phonon thermal conductance of single crystalline SiC, single crystalline ZrB_2, and SiC-ZrB2 interface as a function of strain and temperature and **(b)** percentage change with respect to 500 K value in phonon thermal diffusivity in single crystalline SiC, single crystalline ZrB_2, and SiC-ZrB2 interface as a function of strain and temperature

Fig. 11-(a) shows phononic contribution to thermal conductance as a function of temperature and at 0% and 10% strain values. As shown, phonon thermal conductance of SiC reduces as a function of temperature at both 0% and 10% strain values. However, in the case of ZrB_2 the phononic contribution to thermal conductance increases as function of temperature. This can possibly be attributed to combined sp-sp^2-sp^3 hybridized state of bonds in ZrB_2 (besides highly polarized d orbitals which also lead to spd hybrid bond configuration) instead of the sp^3-hybridized bonds in the case of SiC. The slightly metallic character of bonds in ZrB_2 leads to free

electrons and slightly ionic cores participating in thermal conduction as against in the case of SiC where bond character is strongly covalent with no electrons available for thermal conduction. With increase in temperature the thermal energy in ZrB_2 gets distributed between ionic cores and free electrons. Increased mobility of free electrons at increasing temperature also contributes to ionic core mobility with the remaining thermal energy getting deposited in the acoustic phonon mods leading to increase in phonon thermal conductance. The thermal diffusivity of ZrB_2 increases with temperature (Fig. 11-(b)) indicating a fast redistribution and disposal of energy in phonon modes in ZrB_2. The electronic thermal conductance is also expected to rise (shown later). In the case of SiC, the non-availability of free electrons and strong covalent bonds associated with possible increase in vibration amplitude as well as vibration frequencies due to increased temperatures (shown later) should lead to increase in phonon thermal conductance. However, as shown the phonon thermal conductance reduces with increase in temperature. Due to rigid sp^3 hybridized bonds, the increased thermal energy at higher temperatures leads to increase in phonon frequencies. Much of this increase goes to higher frequency optical phonon modes that do not participate in thermal conduction. The thermal energy in acoustic phonon modes that govern thermal conduction reduces leading to reduction in phonon thermal conductance of SiC. Since SiC does not have free electrons its electron thermal conductance is also expected to reduce as a function of temperature (shown later). Straining in both cases of SiC and ZrB2 leads to reduction in phonon frequencies relative to 0% strain resulting in reduction of phonon thermal conductance with increase in straining. At the ZrB_2-SiC interface the thermal conduction is dominated by bonds that are predominately sp^3 hybridized (only Zr related bonds have metallic character) leading to reduction in phonon thermal conductance with increase in temperature. The value of the interface phononic contribution to thermal conductance lies close to the ZrB_2 value indicating that most of the thermal energy at the interface gets redistributed to free electrons and ionic cores participating in thermal conduction. In essence, the interface has attribute of SiC with phononic thermal conductance reducing with increase in temperature while the thermal conductance mechanism is that of ZrB_2 with thermal energy getting redistributed to ionic cores and free electrons.

An important indicator of the change in lattice vibration amplitude and frequencies of a material is its thermal diffusivity. The phononic contribution to thermal diffusivity is plotted in Fig. 11-(b) at 0% strain value as a function of temperature for all three crystals examined. As shown, with initial increase in temperature thermal diffusivity of all samples follows the similar trend as that of the phononic thermal conductance. Later in the case of ZrB_2, thermal diffusivity starts to reduce with increase in temperature. Thermal diffusivity is an indicator of how fast a material can achieve thermal equilibrium. It incorporates thermal conductivity as well as specific heat capacity of a material. Faster a material achieves thermal equilibrium faster it is able to dispose of any additional heat impingent it. Overall trend in the figure is of reducing thermal diffusivity with increase in temperature as well as with increase in strain.

The observations in Fig. 11 and related arguments are intricately linked with phononic vibration frequencies and average phonon amplitude. To examine the issue further, average phonon amplitude of all systems s a function of temperature increase and strain change is examined in Fig. 12. With increase in temperature, phonon vibration amplitude increases in all

systems. While for SiC and ZrB$_2$, the increase is substantial both as a function of temperature and strain, the interface has a modest increase. Greater thermal energy with increase in temperature and additional strain energy due to increased strain energy either can get absorbed in phonon frequency increase or in phonon vibration amplitude increase. In the case of SiC and ZrB$_2$ the additional energy changes average phonon amplitude significantly. However, due to structural mismatch at the interface, the imposition of thermal energy or strain energy does not change phonon amplitude at the interface appreciably.
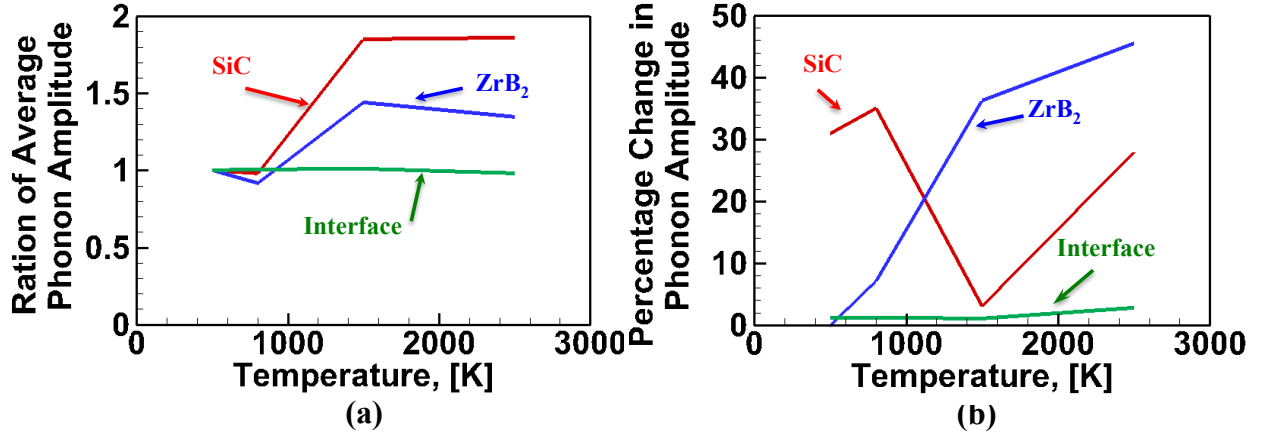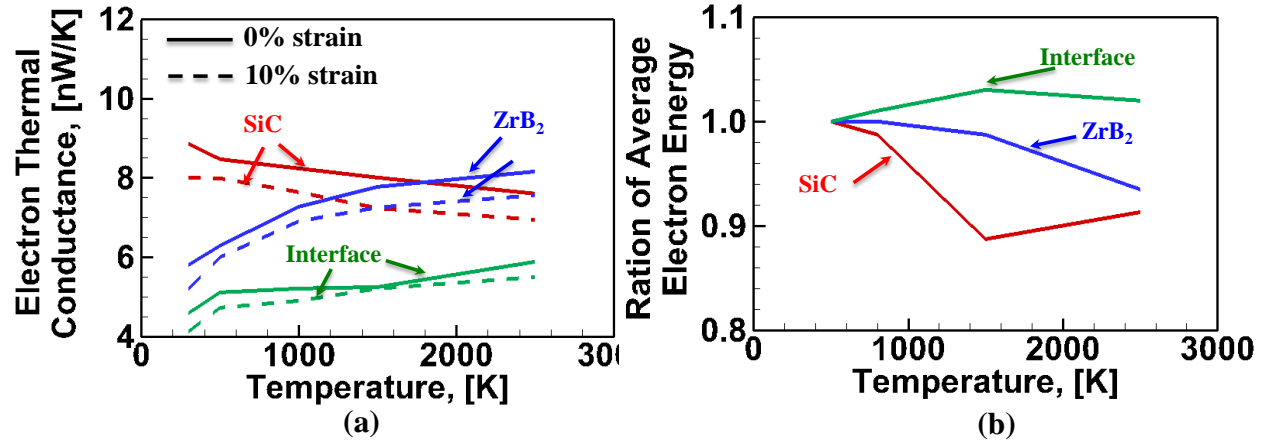

Fig. 12 (a) Ratio of average phonon amplitude at 500 K with that at higher temperatures in the case of ZrB$_2$, SiC, and ZrB$_2$-SiC interface and **(b)** percentage change in average phonon amplitude with straining from 0% to 10% as a function of temperature in the case of ZrB$_2$, SiC, and ZrB$_2$-SiC interface

A combination of Figs. 10 to 12 indicates that temperature related softening of examined materials could be associated with increase in average interatomic distance and overall reduction in thermal diffusivity. With material softening at higher temperatures and the corresponding increase in interatomic distance the average phonon amplitude increases that leads to higher thermal energy absorption capability. Straining, invariably, led to change in phonon amplitude as well as phonon density of states. Both factors combined together to further reduce the thermal diffusivity in materials as a function of temperature. These observations also indicate that by phase mixing it is possible to tune thermal conductance as well as rate of conductive heat transport in a material.

Besides phonon, electrons have been considered to be of importance in thermal conduction especially at high temperatures, [59]. The electron contribution to thermal conduction in the form of electron thermal conductance was calculated using the NEGF formulation described before, Fig. 13. The trend of the electron thermal conductance variation as a function of temperature and strain remains the same as observed in the case of the phonon thermal conductance in the case of SiC and ZrB$_2$. However, interface now shows increase in electron thermal conductance with increase in temperature. The variation with temperature increase shown by the interface electron thermal conductance is also significantly higher in comparison to the one shown by interface phonon thermal conductance. Electron thermal diffusivity also shows a similar trend as phonon

thermal diffusivity (not shown). With softening, the electron thermal conductance shows appreciable increase in the case of interface and ZrB_2. A comparison of thermal diffusivity of electrons and phonons separately at high temperatures indicates that thermal diffusivity contribution of electrons increases at high temperatures to as much as 20% in comparison of about 10% at room temperature. These observations are in line with earlier discussion regarding availability of free electrons in the case of ZrB_2 and interface and non-availability of such electrons in the case of SiC. With increase in temperature electrons get increasingly mobile and with reduced bad gap start to participate significantly in the thermal conduction. Interface formation between SiC and ZrB_2 leads to stronger material with reduced thermal diffusivity but higher electron thermal conductance.

**Figure 13 (a)** Electron thermal conductance of single crystalline SiC, single crystalline ZrB_2, and SiC-ZrB2 interface as a function of strain and temperature and **(b)** ratio of average electron energy at 500 K with that at higher temperatures in the case of ZrB_2, SiC, and ZrB_2-SiC interface

Contribution of ZrB_2 to the interface electron density of states is examined in Fig. 14 using Mulliken analysis. The figure shows change in *d*-orbital electron density of states as a function of temperature at 0% strain. Appreciable change in electron density is found to occur as a function of temperature in the case of interface in comparison to that in the case of ZrB_2. With ZrB_2 structural setup any influence of atomic restructuring occurs by shift in the lighter B atoms. In the case of interface, besides Zr-B bonds (combined sp^2-sp^3 hybridized with *spd* contributions), Si-B (sp^3 hybridized) bonds also participate in shift of B atoms. This behavior of lighter atoms taking more shifts under the influence of external parameters to adjust for the changes in the surrounding may be one factor that can contribute to increasing average electron energy trend with respect to temperature in the case of interface. Another aspect is that interface *d*-orbital electron density of states is distributed over negative as well as positive energy levels. The ZrB_2 electron density of states is distributed over positive energy levels predominantly. Clearly, the delocalized electrons observed in electron density contour at the SiC side of interface in Fig. 15, have significant influence of valence *d*-orbital in the ZrB_2 phase of the interface. Such delocalization imparts metastability to interface and ultimately leads to increase in average electron energy as a function of increase in temperature as well as increase in electron thermal conductance of interface.
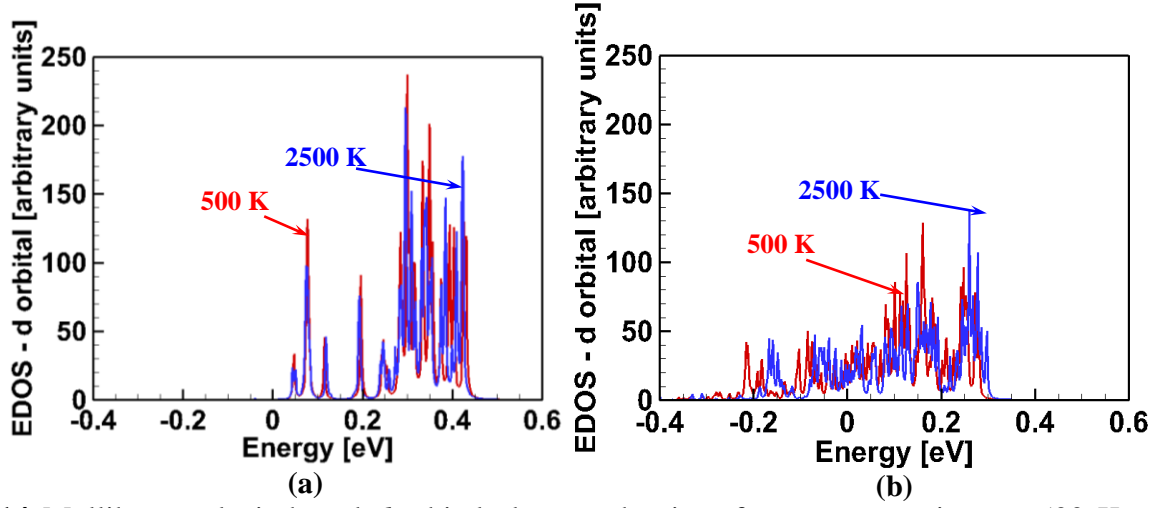
Fig. 14 Mulliken analysis based *d*-orbital electron density of states comparison at 500 K and 2500 K and at 0% strain in the case of **(a)** ZrB$_2$ single crystal and **(b)** ZrB$_2$-SiC interface
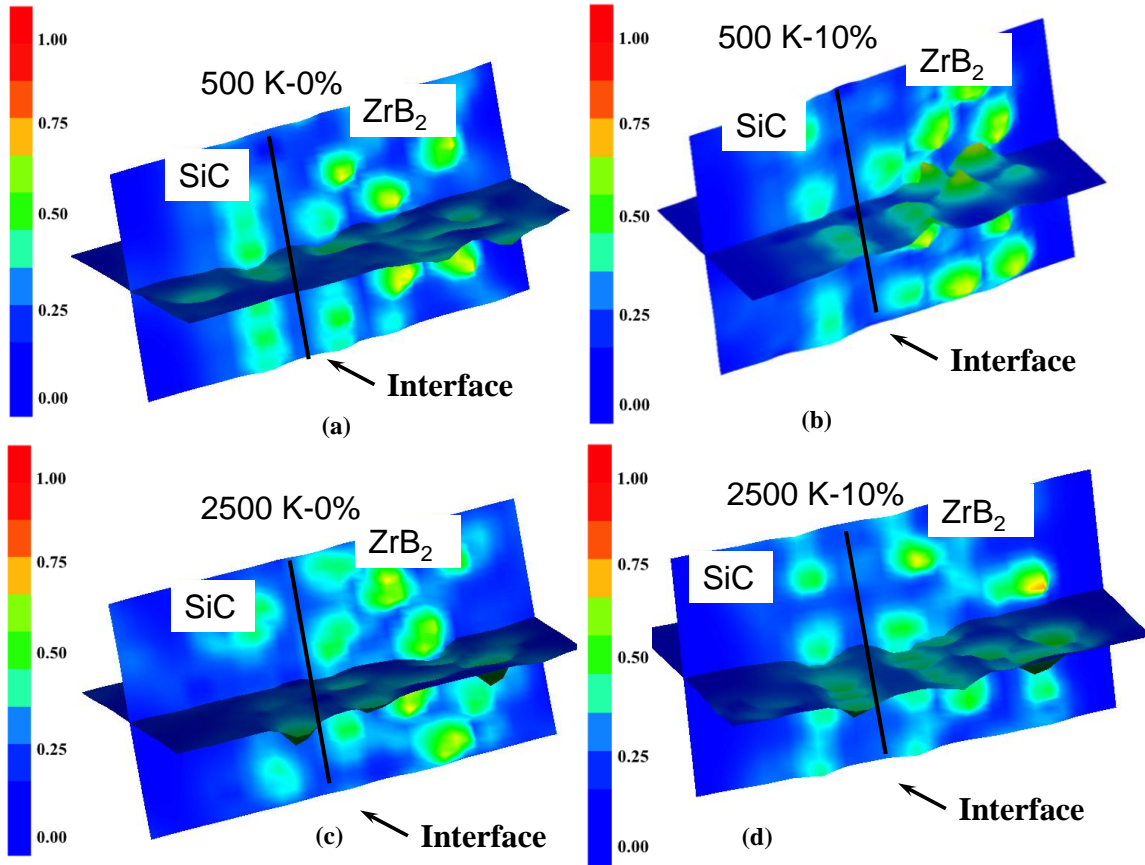
Fig. 15 Electron density contour for ZrB$_2$-SiC interface at **(a)** 300 K and 0% strain, **(b)** 300 K and 10% tensile strain **(c)** at 2500 K and 0% strain and **(d)** at 2500 K and 10% strain.

§2.1.1 SUMMARY

Fundamentally, tunable thermal shock performance of a high temperature material demands high thermal diffusivity combined with high thermal conductivity. A first step in this direction is to be able to examine an interface strength at high temperatures and its correlation with thermal conductivity and thermal diffusivity. Since, high temperature operation involves possible complex nanostructural phase changes in an interface, a quantum mechanical approach to analyze such correlation is necessary. The present work reported such analyses. The most stable <0001>-<111> ZrB_2-SiC interface is chosen for analyses as a function of strain and temperature for correlation between the thermal and mechanical properties.

It is widely known that with temperature increase, ratio of individual contribution of phonons and electrons to overall thermal conductance changes, but very little is known to what extent. The present work sheds some light in this regard for SiC and ZrB_2 single crystals as well as for the SiC-ZrB_2 interface. Earlier, Marshall group [59] have analyzed thermal conduction at high temperatures in a variety of ZrB_2-SiC composites. However, their findings results are at the composite macro level. Findings in this work regarding interface and single crystal thermal-mechanical correlations can significantly help in interpreting their results, especially with regard to the role played by electron thermal conductance. The findings in this work for the first time analyze thermal-mechanical correlations in single crystalline phases and compare those with the behavior of an interface.

Analyses indicate that there is a direct correlation between strength reduction with increase in temperature and the corresponding proportional increase in average interatomic distance in the case of all three samples. The phonon thermal diffusivity shows a direct and proportionate correlation with temperature increase in the case of ZrB_2 and an inverse correlation in the case of SiC and interface, indicating a possibility that in these materials temperature increase may be associated with the changes in the ability to diffuse heat. Thermal conductance is found to have a strong correlation to phonon density of states. The thermal diffusivity, however, is found to be correlated with both phonon amplitude and phonon frequencies. Fundamentally, increased phonon amplitude correlates to increase in specific heat and therefore reduction in thermal diffusivity. Effect of strain is always to reduce phonon density of states and increase the phonon vibration amplitude. Reduction in the density of states leads to reduced thermal conductance and increase in phonon vibration amplitude leads to increased specific heat and reduced thermal diffusivity. Analyses of electron thermal conductance and electron energy change with respect to temperature indicate that electron thermal contributions increase appreciably with temperature. While electrons get delocalized with increase in temperature and strain, their average energy occupation levels increase leading to reduction in their average energy in the case of single crystals. However, the delocalization does not lead to reduction in electron energy levels at the examined interface indicating a metastable state. Examination of change in thermal properties at different mechanical strain levels reveals that the mechanisms of strength and thermal property change with increase in temperature may be similar to the mechanisms responsible for property change with change in applied strain.

### §2.2 FINDINGS FROM CLASSICAL MOLECULAR SIMULATIONS

. Since *ab-initio* approach is limited to small system sizes because of significant computational demand, such simulations are being coupled to approximate classical molecular

simulations to scale up the simulation predictions to realistic microstructure size. Accordingly, the development of *ab-initio* approach was performed together with analyses of interfacial heat transfer as a function of molecular scale morphology. A widely studied material system (Si-Ge) was analyzed in order to standardize the approach in light of available data. In the following salient details of the simulations are presented.

§2.2.1 THERMAL CONDUCTION ANALYSES IN SUPERLATTICES AS A FUNCTION OF STRAIN

Superlattices are nanoscale engineered material system in which the thermal conduction properties could be tailored for applications such as high figure of merit (ZT) thermoelectric, microelectronics, and optoelectronics devices etc. [60] Widely researched superlattices such as $Si/Si_{1-x}Ge_x$, [61-63] GaAs/AlAs, [64] and Bi_2Te_3/Sb_2Te_3, [65] have been observed to have thermal conductivity values much lower than the bulk systems of similar composition. Factors that could be adjusted for tailoring the thermal conductivity of superlattices include the monolayer film thickness, periodicity, heat flow direction, straining, and temperature of operation. Different groups, [61, 62], have worked on experimentally analyzing thermal transport in Si-Ge superlattice thin film structures as a function of the number of superlattice period and thickness. Chen and coworkers analyzed thermal conductivity in superlattice systems using numerical solutions of Boltzmann transport equations (BTE) and molecular dynamics (MD). [66]˙[67] Chen and co-workers [68] performed MD simulations studying the dependence of thermal conductivity on the period length. NEMD analyses of Si-Ge superlattices with unspecified number of periods using Stillinger-Weber potential have been performed to study the dependence of thermal conductivity on the monolayer film thickness. [69, 70]

Thus, analyses so far lack a combined account of factors such as tensile vs. compressive straining, change in number of periods, change in temperature, and change in the monolayer film thickness for a single superlattice material system. Recently, Zhou and coworkers [71] did an analysis of the effect of heat flow direction on thermal conductivity of composite metals. They found that the thermal properties change with the change in heat flow direction. The present work attempts to analyze the effect of tensile vs. compressive straining, change in number of periods, change in temperature, and change in the monolayer film thickness on the thermal conductivity of Si-Ge superlattices.
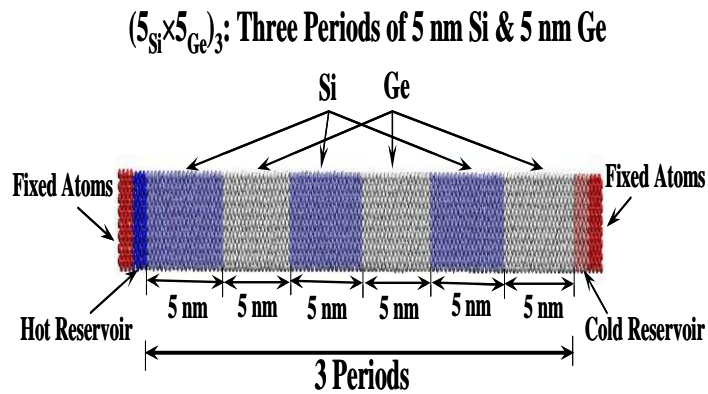
Fig. 16: Terminology for layered structures

NON-EQUILIBRIUM MOLECULAR DYNAMICS

Figure 16 shows the simulation setup and the terminology for the superlattices analyzed in the presented research using NEMD. The simulation supercell is bounded by fixed atomic layers of length equivalent to 25Å, i.e. up to 9 atomic layers on either side, Fig. 16. In order to simulate a thin film structure, PBCs are imposed in the directions transverse to the length of supercells. All layers have <100> orientation along the length of supercells. We chose 4x4 unit cells in transverse direction cross-sectional area, [72]. As shown, a $(5_{Si}\times5_{Ge})_3$ structure represents an interfacial supercell of 5 nm thick Si thin film with 5 nm thick Ge thin film. Subscript 3 denotes that the supercell consists of three periods. In the presented research, supercells with four different thicknesses (2.5nm, 5nm, 7.5nm, 10nm) and three different periods (1, 2, 3) are analyzed at three different temperatures (400 K, 600 K, and 800 K). We can calculate thermal conductivity, k, as

$$k = \frac{\Delta E_{hot} + \Delta E_{cold}}{t_s A \left| \nabla T \right|} . \tag{8}$$

Here, $\nabla T = (\Delta T / L)$ where ΔT is the temperature difference between the hot and cold reservoirs, L is the length of simulation cell, A is the cross-sectional area of the simulation supercell and t_s is the simulation time. To impose a constant heat flux, the hot and cold reservoirs need to be kept at a constant temperature. The energy supplied to the hot and cold reservoirs to maintain a constant temperature is based on momentum conservation scheme [73] and can be calculated from

$$\Delta E = \frac{1}{2} \sum_{i=1}^{N} m_i (v^2_{i,new} - v^2_{i,old}) . \tag{9}$$

Here, $v_{i,old}$ is the old atomic velocity, $v_{i,new}$ is the new atomic velocity after scaling. In addition to computing k, thermal boundary resistance (TBR) across an interface i, R^i_{BD} can be calculated as

$$R^i_{BD} = \left(\Delta T_{int} \right)_i / J , \tag{10}$$

$$J = \frac{1}{A} \frac{\sum_{j=1}^{n} \Delta E(j)}{t_s} . \tag{11}$$

Here, ΔT_{int} represents the temperature drop measured at each interface and J gives the heat flux. To study the effect of strain on the thermal conductivity, we varied the strain by stretching the simulation cell from 10% to -10% with step size of 2% and ran MD simulation at each strain level to calculate the thermal conductivity.

Simulation Setup

The inter-atomic interactions for Si-Ge systems are described by the Tersoff bond-order potential, [74]. During NEMD simulations to compute k at a temperature T, the superlattice system is equilibrated for 200 ps with a time step of 1 femtosecond (fs) in microcanonical (NVE)

ensemble at temperature T. After equilibration, a temperature gradient is established by imposing $T_{hot}=T+30$ K and $T_{cold}=T-30$ K in the hot and the cold reservoir respectively using momentum conservation scheme[73], followed by further equilibration of the computational supercell for 500 ps. During this equilibration procedure, at each time step the values of k are calculated using Eq. (8). Calculations showed that the heat flux imposed on the superlattices by fixing up the hot and cold reservoir temperatures took approximately from 200 to 300 ps to get stabilized. For calculating temperature profile along the supercell length, each supercell was divided into thin slabs of length a little larger than both Si and Ge lattice constant. Once the values of k converge, the temperature profile along the length of the supercells is obtained by calculating average temperature of each slab based on the total kinetic energy of all atoms in the slab averaged over 100 ps.
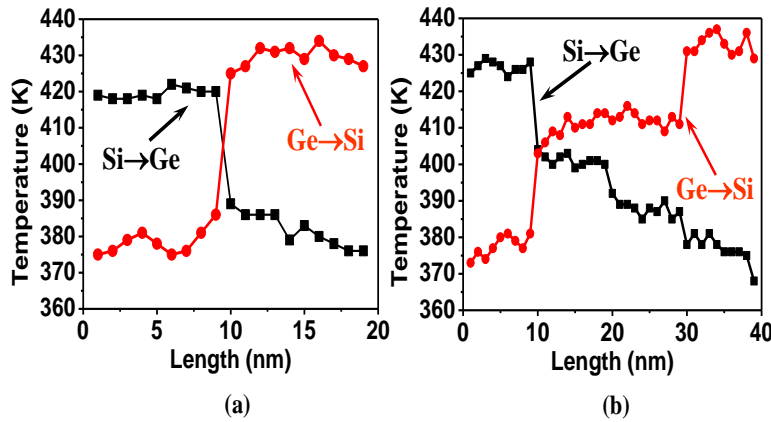

Fig. 17: Temperature profile for (a) $(10_{si}\times10_{ge})_1$ and $(10_{ge}\times10_{si})_1$, and (b) $(10_{si}\times10_{ge})_2$ and $(10_{ge}\times10_{si})_2$ simulation systems

RESULTS

Figure 17 displays the temperature profile obtained along the length of the $(10_{Si}\times10_{Ge})_{x=1,\,2}$ and $(10_{Ge}\times10_{Si})_{x=1,\,2}$ simulation systems plotted for increasing period values. Fig. 2(a) shows temperature profile for $(10_{Si}\times10_{Ge})_1$ and $(10_{Ge}\times10_{Si})_1$ superlattices after convergence in k values corresponding to $T=400$ K. As shown in the curves in Fig. 17(a), a steep drop in temperature is observed at the interface of Si-Ge at the position corresponding to 10 nm. Such drop in the temperature is attributed to the thermal boundary resistance offered by the interface and is observed to be different for the superlattice with different directions of heat current. This directional dependence is discussed later in section. Fig. 17 (b) shows the temperature drop across interfaces of $(10_{Si}\times10_{Ge})_2$ and $(10_{Ge}\times10_{Si})_2$ which also clearly shows the effect of interface boundary resistance. Another important aspect of interfacial conduction observed in Fig. 17 is the non-linear behavior of interfaces in offering resistance to heat flow as the number of interfaces increase. Calculations done on the basis of temperature drop recorded at each interface leads to the observation that the total TBR does not increase linearly with the increase in the number of interfaces, as suggested by Ref. [75].

Thermal Conductivity as a Function of Superlattice Period, Film Thickness, Temperature and Strain

We examined the variation of thermal conductivity of $(5_{Si} \times 5_{Ge})_{1,2, and 3}$ and $(10_{Si} x 10_{Ge})_{1,2, and 3}$ superlattices with increase in number of periods at temperatures 400K, 600K and 800K. Thermal conductivity increases with increase in monolayer thickness and with increase in number of periods. The rate of change of thermal conductivity with increase in the number of periods is found to be higher for thicker monolayer films. This is because, there are two factors competing with each other: (1) number of interfaces increase leading to higher cumulative R_{BD}, and (2) length of the superlattice system increase leading to a drop in the overall temperature gradient. For higher superlattice period thickness, i.e. with thicker monolayer films, the latter dominates over the former by a significant proportion. Accordingly, there is a steeper increase in the thermal conductivity value for higher period thickness.
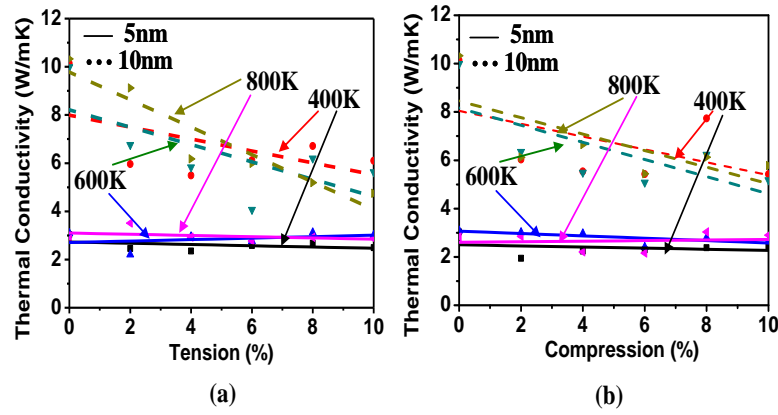
Fig. 18: Thermal conductivity as a function of strain at different temperatures for $(5_{si} x 5_{ge})_3$, $(10_{si} x 10_{ge})_3$ structures

Effect of Straining on Thermal Conductivity as a Function of Temperature

Figure 18 displays the thermal conductivity of $(5_{Si} x 5_{Ge})_3$ and $(10_{Si} x 10_{Ge})_3$ systems as a function of temperature at different strain levels. Both compressive and tensile strain causes the thermal conductivity of superlattices to decrease. This trend is different from the earlier reported analyses in literature [75-77] regarding the effect of strain on the thermal conductivity. We conjecture that this difference is attributable to simulations being performed near or above Debye temperature values in our case. With the increase in the number of periods, the decrease in thermal conductivity is higher for higher strain and this trend is observed at all three temperatures: 400K, 600K and 800K. It is observed that the straining has insignificant effect on the thermal conductivity of superlattices with 5 nm monolayer thickness, as we approach thin film limit. Similarly, when tensile strain is applied, atomic distance increases, phonon relaxation time increases and structure stiffness decreases. But, an increase in the period thickness and periodicity causes the nucleation of structural defects, [62] (identified as deviation from perfect single crystal structure). The formation of structural defects is more pronounced at high temperatures, which is experienced in this study. The scattering at the defects and dislocations provide additional resistance to the flow of heat current through the material system, which leads

to a reduction in the thermal conductivity with an increase in tensile strain, [75]. It is also clear from the figures that the effect of straining is more pronounced at larger period thickness, which is again due to chances of dislocation nucleation being higher for higher period thickness. This decrease of thermal conductivity due to strain is seen to increase with an increase in the number of periods, at all period thicknesses.

Effect of Heat Flow Direction Reversal on Thermal Conductivity Values

Figure 19 shows a comparison of thermal conductivity as a function of temperature and heat flow direction for $(7.5_{Si} \times 7.5_{Ge})_3$ and $(7.5_{Ge} \times 7.5_{Si})_3$ superlattices, and for $(10_{Si} \times 10_{Ge})_3$ and $(10_{Ge} \times 10_{Si})_3$ superlattices. As shown, with an increase in the period thickness, the effect of the reversal in the heat flow direction becomes significant. This behavior can be attributed to the change in the frequency of the heat carrying phonons with the change in the heat flow direction. For Si→Ge system, heat transfer characteristics are dominated by the phonons in Si monolayer whereas in Ge→Si, the heat transfer is determined by the phonons in Ge monolayer. Owing to a large atomic mass difference between Si and Ge, which reflects both in terms of large acoustic mismatch across Si-Ge layer and also in the difference in the frequency of Si and Ge phonons, the thermal resistance offered by an interface to a particular type of phonon varies. This difference grows with an increase in the number of periods and results in a larger drop in thermal conductivity value for Ge→Si system, when compared with Si→Ge system.
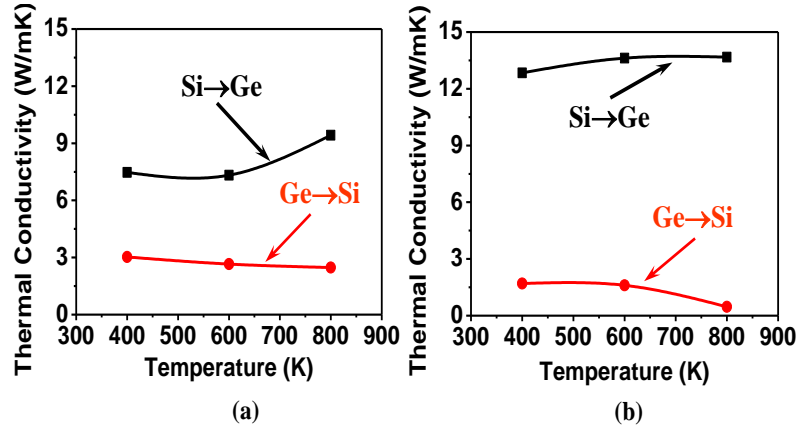

Fig. 19: Dependence of thermal conductivity on heat flow direction as a function of temperature for (a) $(7.5_{si} \times 7.5_{ge})_4$ and $(7.5_{ge} \times 7.5_{si})_4$ superlattices, and (b) $(10_{si} \times 10_{ge})_4$ and $(10_{ge} \times 10_{si})_4$ superlattices

§2.2.2 THERMAL CONDUCTION IN BIOMIMETIC COMPOSITES AS A FUNCTION OF STRAIN

The MD based thermal conductivity calculations in the case of biomimetic nanocomposites are based on the same framework used in the case of superlattices. Biomimetic nanocomposites with nanostructures in the form of nanoparticles and nanowires embedded in a host matrix material differ from conventional composite materials in their thermal and mechanical properties due to exceptionally high surface to volume ratio of the nanostructures acting as reinforcing phase. Atomistic analyses of the biomimetic nanocomposite thermal behavior are limited. Jeng and coworkers [78] have used Monte Carlo simulations to study the phonon transport and thermal

conductivity reduction in the biomimetic nanocomposites with Si nanoparticle embedded in Ge host. Similar Monte Carlo analyses for the nanocomposites with Si tubular nanowires in Ge host have been performed by Yang and group [79]. In a recent work, Huang and group [80] have used molecular dynamics (MD) simulations to analyze similar systems as analyzed by Yang and group [79]. Yang and group [81] have theoretically studied phonon thermal conductivity of periodic two-dimensional nanocomposites with nanowires embedded in a host semiconductor material using phonon Boltzmann equation. They have concluded that the thermal conductivity of nanocomposites is always higher than that of a superlattice with the same characteristic thickness. The difference reduces as the dimensions of the two types of materials are reduced. A single conclusion common to all analyses has been that the reason behind biomimetic nanocomposites displaying low thermal conductivities is high percentage of atoms in the interfaces leading to significant phonon scattering. Interface atom fraction in the superlattices is usually lower than that in the biomimetic nanocomposites. Since structurally the superlattices and the biomimetic nanocomposites are significantly different, their response to externally imposed mechanical straining should also be different. By a judicious combination of applied straining and morphology it should be possible to tailor the thermal conductivity of both types of materials. With this view, the present investigation focuses on understanding thermal behavior of a set of Si-Ge biomimetic nanocomposites using non-equilibrium molecular dynamics (NEMD) simulations at three different temperatures (400 K, 600 K, and 800 K) and at strain levels varying between -10% and 10%
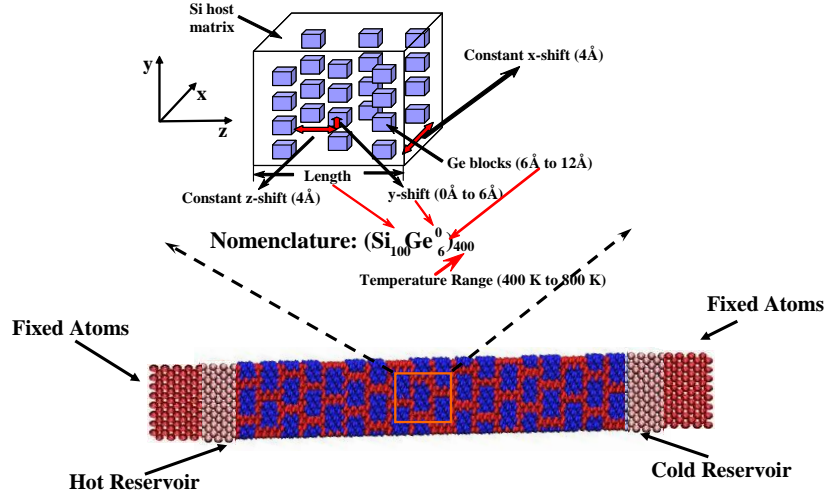

Fig. 20 Simulation setup and terminology for the nanocomposite structures analyzed for thermal conduction. The staggered arrangement of Ge blocks inside Si host matrix is displayed along with various parameters considered in this study

Figure 20 displays the staggered arrangement of Ge blocks inside Si host matrix, highlighting various parameters that were varied to study their effect on the overall thermal conductivity of the biomimetic nanocomposites. The nomenclature $(Si_{100}Ge^{0}_{6})_{400}$ shown in the Fig. 20 helps in identifying each biomimetic nanocomposite analyzed. The subscript 100 on Si represents the thickness of the nanocomposite with Ge cubic blocks of size 6 Å as indicated by the Ge subscript of 6. The superscript 0 to Ge represents the Y-shift (extent to which a Ge particle is shifted in the

y-direction with respect to an adjacent Ge particle). In the present work, nanocomposites with three different thicknesses: 10nm, 20nm and 30nm are analyzed. For each thickness, nanocomposites with three different Ge block sizes: 6 Å, 9 Å, and 12 Å are generated. Four values of Y-shift: 0 Å, 2 Å, 4 Å, and 6 Å are used for each nanocomposite thickness and for each Ge block size. It is made sure that all nanocomposites have equal number of Ge blocks at a cross-sectional view in the x-y plane. As shown in Fig. 20, the simulation supercell is bounded by fixed atomic layers of thickness equivalent to 25Å, i.e. up to 9 atomic layers on either side. Further increase in the thickness of fixed atomic layers did not change the presented results. Periodic boundary conditions (PBCs) are imposed in the directions transverse to the thickness of composite supercells to be able to simulate a thin film structure. Both, Si and Ge have <100> orientation along the thickness. A nanocomposite configuration may affect the lattice constant values of both Si and Ge. Based on the analyses by Volz and coworkers [82], lattice parameters for Si, a_{Si}=5.43 Å and for Ge, a_{Ge}=5.657 Å are used.

**Effect of Straining as a Function of Temperature**
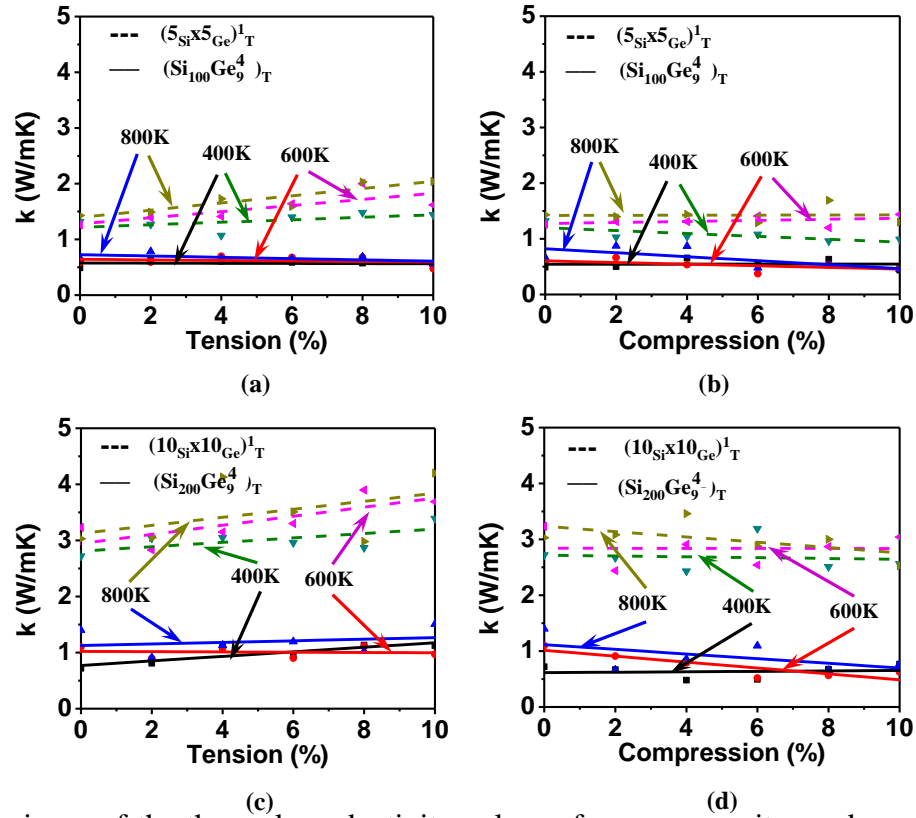
Fig. 21 Comparisons of the thermal conductivity values of nanocomposites and superlattices of equal thickness as a function of strain. Plots are (**a**) for $Si_{100}Ge^4_9$ and $(5_{Si}x5_{Ge})_1$ under tension, (**b**) for $Si_{100}Ge^4_9$ and $(5_{Si}x5_{Ge})_1$ under compression, (**c**) for $Si_{200}Ge^4_9$ and $(10_{Si}x10_{Ge})_1$ under tension, and (**d**) for $Si_{200}Ge^4_9$ and $(10_{Si}x10_{Ge})_1$ under compression at 400 K, 600 K and 800 K.

Figure 21 displays the thermal conductivity variation of $Si_{100}Ge^4_9$ and $Si_{200}Ge^4_9$ nanocomposites as a function of tensile and compressive straining at three different temperatures: 400K, 600K and 800K. Variation of the thermal conductivity of the superlattices: $(5_{Si}x5_{Ge})_1$ and $(10_{Si}x10_{Ge})_1$, [83], with comparable thickness has been plotted (dashed lines) along

the nanocomposite thermal conductivity values in order to offer a comparison. As shown, a linear fit to the data on thermal conductivity for the nanocomposites as well as the superlattices can be obtained. It is observed that the straining has insignificant effect on the thermal conductivity of the nanocomposites with 10 nm thickness and slightly affects the thermal conductivity of the nanocomposites with 20 nm thickness. Overall, however, the thermal conductivity shows a stronger dependence on strain in the case of superlattices when compared to the nanocomposites, [83]. The superlattices with comparable thickness show an increase in thermal conductivity values as a function of tensile strain and decrease in the values as a function of compressive strain. This difference of the effect of straining on the thermal conductivity of nanocomposites when compared with superlattices can be explained from the phonon spectral density plots. In superlattice phonon spectrum, (not shown here, can be observed in our Journal of Physics Publication pointed out at first page), we have sharply defined peaks corresponding to certain frequencies which dominate the heat transfer. Correspondingly, only a limited frequencies are the most significant contributors to the heat transfer. On the contrary, in the nanocomposites there are no sharply defined peaks in the phonon spectrum. Accordingly, there is a wide spectrum of phonon frequencies with equivalent spectral densities, which carry the heat current across. Therefore, the reduction or increase in the interatomic distance caused by straining and the ensuing gain or loss in the stiffness, respectively, can affect superlattice phonon spectrum more owing to the dominance of a limited frequencies. In the nanocomposites, the effect is subdued, because the heat transfer is distributed across a much larger spectrum of wavelengths, Fig. 22. This difference of heat carrier phonons in the nanocomposites, when compared to those in superlattices leads to the observed difference in the variations of thermal conductivity shown in Fig. 6. To further explain the variation of thermal conductivity with straining, we can write k as, [75, 77],

$$k = \frac{1}{3} C v^2 \tau_{ph} \qquad \text{Or} \qquad k = \frac{1}{3} C r_{ij}^2 \frac{g}{m} \tau_{ph} . \qquad (12)$$

Here τ_{ph} gives phonon-phonon interaction or phonon relaxation time, g represents the stiffness constant of the atomic structure, and m gives the mass of atoms. In the above equation, the relations $l = v \tau_{ph}$ and $v = r_{ij} \sqrt{g/m}$ are used. Here, r_{ij} represents the average interatomic distance. It can be shown that an increase in the compression causes a decrease in r_{ij} equivalently for both superlattices and nanocomposites.

(a)   (b)
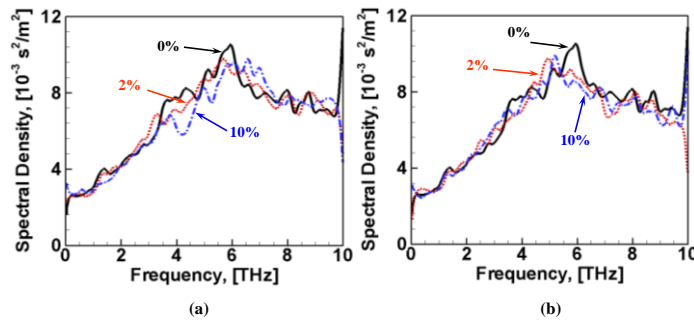
Figure 22 A comparison of the phonon spectral density at different strain levels for $Si_{100}Ge^4_9$ nanocomposite at 400 K, under **(a)** tension, and **(b)** compression

As shown in Fig. 23, the radial distribution functions (RDFs) for the nanocomposites are not significantly affected by straining. Therefore, tension or compression affects superlattice thermal conductivity in a more significant manner. It is also clear from the Fig. 21 that the effect of straining is more pronounced at larger period thickness for superlattices and higher thickness nanocomposites, which can be attributed to chances of defect nucleation being higher for higher period thickness. In addition, for higher thickness nanocomposites, the interfacial atom fraction reduced when compared to that in smaller thickness nanocomposites (e.g. 10 nm here). This directly leads to higher effect of straining in higher thickness nanocomposites.
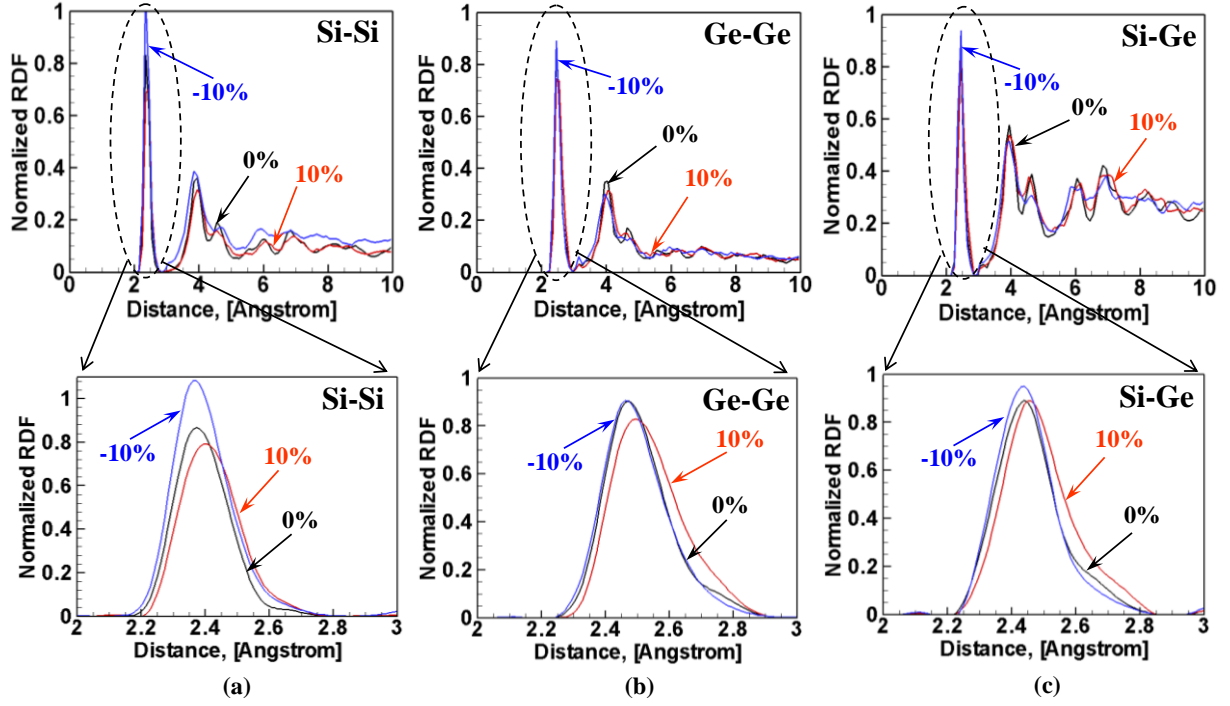
Figure 23 A comparison of the **(a)** Si-Si, **(b)** Ge-Ge, and **(c)** Si-Ge normalized radial distribution functions (RDF) at different strain levels for $Si_{100}Ge^4_9$ nanocomposite at 400 K

The reduction in the interatomic distance due to compression or increase in the interatomic distance due to tension significantly affects phonon relaxation time, τ_{ph}. Such changes in the interatomic distances also lead to the corresponding changes in the lattice stiffness. Since, nanocomposites have a significantly high interface atom fraction, the extent of r_{ij} reduction or increase with tension or compression, respectively, is limited when compared to that in superlattices, Fig. 23.

REFERENCES TO TEXT IN THE REPORT

1.   *Asheghi, M., M.N. Touzelbaev, K.E. Goodson, Y.K. Leung, and S.S. Wong, Temperature-dependent thermal conductivity of single-crystal silicon layers in SOI substrates. Journal of Heat Transfer-Transactions of the Asme, 1998. **120**(1): p. 30-36.*

2.   *Asheghi, M., K. Kurabayashi, R. Kasnavi, and K.E. Goodson, Thermal conduction in doped single-crystal silicon films. Journal of Applied Physics, 2002. **91**(8): p. 5079-5088.*

3.   *Asheghi, M., Y.K. Leung, S.S. Wong, and K.E. Goodson, Phonon-boundary scattering in thin silicon layers. Applied Physics Letters, 1997. **71**(13): p. 1798-1800.*

4.   *Narayanaswamy, A. and N. Gu, Heat Transfer From Freely Suspended Bimaterial Microcantilevers. Journal of Heat Transfer. **133**(4): p. 042401-6.*

5.   *von Arx, M., O. Paul, and H. Baltes, Process-dependent thin-film thermal conductivities for thermal CMOS MEMS. Journal of Microelectromechanical Systems, 2000. **9**(1): p. 136-145.*

6.   *Tai, Y.C., C.H. Mastrangelo, and R.S. Muller, Thermal conductivity of heavily doped low-pressure chemical vapor deposited polycrystalline silicon films. Journal of Applied Physics, 1988. **63**(5): p. 1442-1447.*

7.   *Tai, Y.C., C.H. Mastrangelo, and R.S. Muller. Thermal conductivity of heavily doped LPCVD polysilicon. in Electron Devices Meeting, 1987 International. 1987.*

8.   *McConnell, A.D., S. Uma, and K.E. Goodson, Thermal conductivity of doped polysilicon layers. Journal of Microelectromechanical Systems, 2001. **10**(3): p. 360-369.*

9.   *Irace, A. and P.M. Sarro, Measurement of thermal conductivity and diffusivity of single and multilayer membranes. Sensors and Actuators a-Physical, 1999. **76**(1-3): p. 323-328.*

10.   *Graham, S., B. Olson, C. Wong, and E. Piekos, The effects of processing conditions on the thermal conductivity of polycrystalline silicon films. Electronic and Photonic Packaging, Electrical Systems and Photonic Design and Nanotechnology - 2003, 2003: p. 455-459.*

11.   *Uma, S., A.D. McConnell, M. Asheghi, K. Kurabayashi, and K.E. Goodson, Temperature-dependent thermal conductivity of undoped polycrystalline silicon layers. International Journal of Thermophysics, 2001. **22**(2): p. 605-616.*

12.   *Li, W.B., J.L. Henshall, R.M. Hooper, and K.E. Easterling, The mechanisms of indentation creep. Acta Metallurgica et Materialia, 1991. **39**(12): p. 3099-3110.*

13.   *Chudoba, T. and F. Richter, Investigation of creep behaviour under load during indentation experiments and its influence on hardness and modulus results. Surface and Coatings Technology, 2001. **148**(2-3): p. 191-198.*

14.   *Li, H. and A.H.W. Ngan, Size Effects of Nanoindentation Creep. Journal of Materials Research, 2004. **19**(2): p. 513-522.*

15.   *Herring, C., Diffusional Viscosity of a Polycrystalline Solid. Journal of Applied Physics, 1950. **21**(5): p. 437-445.*

16.   *Coble, R.L., A Model for Boundary Diffusion Controlled Creep in Polycrystalline Materials. Journal of Applied Physics, 1963. **34**(6): p. 1679-1682.*

17.   *Lifshitz, I.M., On the Theory of Diffusion-Viscous Flow of Polycrystalline Bodies. Soviet Physics Jetp-Ussr, 1963. **17**(4): p. 909-920.*

18.   *Weertman, J., Trans. ASM, 1968. **61**: p. 681-694.*

19.   *Nix, W.D. and B. Ilschner. in Proc. 5th Int. Conf. on the Strength of Metals and Alloys (ICSMA 5). 1980. Oxford: Pergamon Press.*

20.   *Sherby, O.D. and P.M. Burke, Prog. Mater. Sci., 1968. **13**: p. 323-390.*

21.	Li, J.C.M., K.H.J. Buschow, W.C. Robert, C.F. Merton, I. Bernard, J.K. Edward, M. Subhash, and V. Patrick, *Creep by Indentation, in Encyclopedia of Materials: Science and Technology*2001, Elsevier: Oxford. p. 1765-1767.

22.	Feng, G. and A.H.W. Ngan, *Creep and strain burst in indium and aluminium during nanoindentation.* Scripta Materialia, 2001. **45**(8): p. 971-976.

23.	Cao, Z.H., P.Y. Li, H.M. Lu, Y.L. Huang, Y.C. Zhou, and X.K. Meng, *Indentation size effects on the creep behavior of nanocrystalline tetragonal Ta films.* Scripta Materialia, 2009. **60**(6): p. 415-418.

24.	Mayo, M.J. and W.D. Nix, *A micro-indentation study of superplasticity in Pb, Sn, and Sn-38 wt% Pb.* Acta Metallurgica, 1988. **36**(8): p. 2183-2192.

25.	Lucas, B. and W. Oliver, *Indentation power-law creep of high-purity indium.* Metallurgical and Materials Transactions A, 1999. **30**(3): p. 601-610.

26.	Asif, S.A.S. and J.B. Pethica, *Nanoindentation creep of single-crystal tungsten and gallium arsenide*, 1997, Taylor & Francis. p. 1105 - 1118.

27.	Zong, Z. and W. Soboyejo, *Indentation size effects in face centered cubic single crystal thin films.* Materials Science and Engineering: A, 2005. **404**(1-2): p. 281-290.

28.	Durst, K., M. Goken, and G.M. Pharr, *Indentation size effect in spherical and pyramidal indentations.* Journal of Physics D: Applied Physics, 2008. **41**(7): p. 074005.

29.	Durst, K., B. Backes, O. Franke, and M. Göken, *Indentation size effect in metallic materials: Modeling strength from pop-in to macroscopic hardness using geometrically necessary dislocations.* Acta Materialia, 2006. **54**(9): p. 2547-2555.

30.	Li, H. and A.H.W. Ngan, *Indentation size effects on the strain rate sensitivity of nanocrystalline Ni-25at.%Al thin films.* Scripta Materialia, 2005. **52**(9): p. 827-831.

31.	Jan, V., F. Dorcakova, J. Dusza, and M. Bartsch, *Indentation creep of free-standing EB-PVD thermal barrier coatings.* Journal of the European Ceramic Society, 2008. **28**(1): p. 241-246.

32.	Chollon, G., J.M. Vallerot, D. Helary, and S. Jouannigot, *Structural and textural changes of CVD-SiC to indentation, high temperature creep and irradiation.* Journal of the European Ceramic Society, 2007. **27**(2-3): p. 1503-1511.

33.	Janakiraman, N. and F. Aldinger, *Yielding, strain hardening, and creep under nanoindentation of precursor-derived Si-C-N ceramics.* J. Am. Ceram. Soc., 2010. **93**(3): p. 821-829.

34.	Janakiraman, N. and F. Aldinger, *Indentation analyses of elastic and plastic deformation of precursor derived Si-C-N ceramics.* J. Eur. Ceram. Soc., 2010. **30**(3): p. 775-785.

35.	Olbricht, J., A. Yawny, M.L. Young, and G. Eggeler, *Mechanical and microstructural observations during compression creep of a short fiber reinforced AlMg metal matrix composite.* Materials Science and Engineering: A, 2009. **510-511**: p. 407-412.

36.	Khan, K.B., T.R.G. Kutty, and M.K. Surappa, *Hot hardness and indentation creep study on Al-5% Mg alloy matrix-B4C particle reinforced composites.* Materials Science and Engineering: A, 2006. **427**(1-2): p. 76-82.

37.	Medved', A.I. and A.E. Bryukhanov, *The variation of Young's modulus and the hardness with tempering of some quenched chromium steels* Metal Science and Heat Treatment, 2004. **11**(9): p. 706-708.

38.	Cheng, Y.-T. and C.-M. Cheng, *Scaling, dimensional analysis, and indentation measurements.* Materials Science and Engineering: R: Reports, 2004. **44**(4-5): p. 91-149.

39.   Christian, J.W., *The Theory of Transformations in Metals and Alloys, 1975, Pergamon Press: Oxford, UK. p. 81.*

40.   Ashby, M.F. and H.J. Frost, *The kinetics of plastic deformation above 0K, in constitutive Equations in Plasticity, A.S. Argon, Editor 1975, MIT Press: Cambridge, MA. p. 119.*

41.   Puthoff, J.B., J.E. Jakes, H. Cao, and D.S. Stone, *Investigation of thermally activated deformation in amorphous PMMA and Zr-Cu-Al bulk metallic glasses with broadband nanoindentation creep. Journal of Materials Research, 2009.* **24**(3): p. 1279-1290.

42.   Losego, M.D., M.E. Grady, N.R. Sottos, D.G. Cahill, and P.V. Braun, *Effects of chemical bonding on heat transport across interfaces. Nature Materials, 2012(PUBLISHED ONLINE: 22 APRIL 2012 | DOI: 10.1038/NMAT3303).*

43.   Samvedi, V. and V. Tomar, *An ab-initio study of coupling between electronic and phononic contribution to stress dependent thermal conductivity of Au, Si, and SiC. Journal of Nanomechanics and Micromechanics. Submitted February 1, 2012; accepted March 9, 2012; posted ahead of print March 12, 2012. doi:10.1061/(ASCE)NM.2153-5477.0000046, 2012.*

44.   Kadanoff, L.P. and G. Baym, *Quantum statistical mechanics: Green's function methods in equilibrium and non-equilibrium problems1962, New York: W.A. Benjamin.*

45.   Keldysh, L.V., *Diagram technique for nonequilibrium processes. Soviet Phys.JETP, 1965.* **20**(4): p. 1018-1026.

46.   Langreth, D.C., *Linear and non-linear electron transport in solids, 1976, vol. 17 of NATO Advanced Study Institute Series: Series B, pp. 3-18. New York: Plenum Press, 1976.*

47.   Mahan, G.D., *Many-Particle physics. Physics of Solids and Liquids1990: New York: Plenum Press, 2nd edition.*

48.   Haug, H. and A.-P. Jauho, *Quantum kinetics in transport and optics of semiconductors1996: Springer, Berlin.*

49.   Meir, Y. and N.S. Wingreen, *Phys. Rev. Lett., 1992.* **68**(2512-2517).

50.   Wang, J.-S., J. Wang, and N. Zeng, *Nonequilibrium Green's function approach to mesoscopic thermal transport. Physical Review B, 2006.* **74**: p. 033408 (4 pp).

51.   Zhang, W., T.S. Fisher, and N. Mingo, *The atomistic Green's function method: An efficient simulation approach for nanoscale phonon transport. Numerical Heat Transfer, Part B: Fundamentals, 2007.* **51: 4**: p. 333-349.

52.   Wang, J.-S., N. Zeng, J. Wang, and C.K. Gan, *Nonequilibrium Green's function method for thermal transport in junctions. Phys. Rev. E, 2007.* **75**: p. 061128 (15pp).

53.   Xu, Y., J.S. Wang, W. Duan, B.-L. Gu, and B. Li, *Nonequilibrium Green's function method for phonon-phonon interactions and ballistic diffusive thermal transport. Phys. Rev. B, 2008.* **78**: p. 224303 (9 pp).

54.   Hopkins, P.E., P.M. Norris, M.S. Tsegaye, and A.W. Ghosh, *Extracting phonon thermla conductance across atomic junctions: Nonequilibrium Green's function approach compared to semiclassical methods. J. Appl. Phys., 2009.* **106**: p. 063503 (11 pp).

55.   Zhang, L., P. Kenblinski, J.-S. Wang, and B. Li, *Interfacial thermal transport in atomic junctions. Phys. Rev. B, 2011.* **83**: p. 064303 (9 pp).

56.   Trivedi, R., P.-L. Liu, R. Roucka, A.V.G. Chizmeshya, I. Tsong, and J. Kouvetakis, *Mismatched heteroepitaxy of tetrahedral semiconductors with Si via ZrB2 templates. Chemistry of Materials, 2005.* **17**(18): p. 4647-4652.

57.   Valiev, M., E.J. Bylaska, N. Govind, K. Kowalski, T.P. Straatsma, H.J.J. van Dam, D. Wang, J. Nieplocha, E. Apra, T.L. Windus, and W.A. de Jong, *NWChem: a comprehensive and scalable open-source solution for large scale molecular simulations.* Comput. Phys. Commun., 2010. **181**: p. 1477-1497.

58.   Fahrenholtz, W.G., G.E. Hilmas, I.G. Talmy, and J.A. Zaykoski, *Refractory diborides of zirconium and hafnium.* J. Am. Ceram. Soc. , 2007. **90**(5): p. 1347-1364.

59.   Zhang, L., D.A. Pejakovic, J. Marschall, and M. Gasch, *Thermal and electrical transport properties of spark plasma-sintered HfB2 and ZrB2 ceramic.* J. Amer. Ceram. Soc., 2011. **94**(8): p. 2562-2570.

60.   Cahill, D.G., W.K. Ford, K.E. Goodson, G.D. Mahan, A. Majumdar, H.J. Maris, R. Merlin, and S.R. Phillpot, *Nanoscale thermal transport.* J. Appl. Phys., 2003. **93**(2): p. 793.

61.   Borca-Tasciuc, T., W. Liu, J. Liu, Z. Taofang, D.W. Song, C.D. Moore, G. Chen, K.L. Wang, M.S. Goorsky, T. Radetic, R. Gronsky, T. Koga, and M.S. Dresselhaus, *Thermal conductivity of symmetrically strained Si/Ge superlattices.* Superlattices and Microstructures, 2000. **28**(3): p. 199-206.

62.   Lee, S.-M., D.G. Cahill, and R. Venkatasubramanian, *Thermal conductivity of Si-Ge superlattices.* Appl Phys. Lett., 1997. **70**(22): p. 2957-2959.

63.   Huxtable, S.T., A.R. Abramson, C.-L. Tien, A. Majumdar, C. LaBounty, X. Fan, G. Zeng, J.E. Bowers, A. Shakouri, and E.T. Croke, *Thermal conductivity of Si/SiGe and SiGe/SiGe superlattices.* Appl Phys. Lett., 2002. **80**(10).

64.   Yu, X.Y., G. Chen, A. Verma, and J.S. Smith, *Temperature dependence of thermophysical properties of GaAs/AlAs periodic structure.* Appl Phys. Lett., 1995. **67**(24).

65.   Venkatasubramanian, R., *Lattice thermal conductivity reduction and phonon localization like behavior in superlattice structures.* Phys. Rev. B, 2000. **61**(4): p. 3091-3097.

66.   Chen, G. and M. Neagu, *Thermal conductivity and heat transfer in superlattices.* Appl Phys. Lett., 1997. **71**(19): p. 2761-2763.

67.   Volz, S., J.B. Saulnier, G. Chen, and P. Beauchamp, *Computation of thermal conductivity of Si/Ge superlattices by molecular dynamics techniques.* Microelectronics Journal, 2000. **31**: p. 815-819.

68.   Chen, Y., D. Li, J.R. Lukes, Z. Ni, and M. Chen, *Minimum superlattice thermal conductivity from molecular dynamics.* Physical Review B, 2005. **72**(174302): p. 1-6.

69.   Landry, E.S., A.J.H. Mcgauhey, and M.I. Hussein, *Molecular dynamics prediction of the thermal conductivity of Si/Ge superlattices.* Proceedings of HT2007 ASME-JSME Thermal engineering summer heat transfer conference, 2007.

70.   Srinivasan, S. and R.S. Miller, *On parallel nonequilibrium molecular dynamics simulations of heat conduction in heterogeneous materials with three-body potentials: Si/Ge superlattice.* Num. Heat Transfer, Part B, 2007. **52**: p. 297-321.

71.   Zhou, Y., B. Anglin, and A. Strachan, *Phonon thermal conductivity in nanolaminated composite metals via molecular dynamics.* The Journal of Chemical Physics, 2007. **127**(184702): p. 1-11.

72.   Schelling, P.K., S.R. Phillpot, and P. Keblinski, *Comparison of atomic-level simulation methods for computing thermal conductivity.* Physical Review B, 2002. **65**(144306): p. 1-12.

73. *Huang, Z. and Z. Tang, Evaluation of momentum conservation influence in non-equilibrium molecular dynamics methods to compute thermal conductivity. Physica B, 2006. **373**: p. 291-296.*

74. *Tersoff, J., Modeling solid-state chemistry: Interatomic potentials for multicomponent systems. Phys. Rev. B (Rapid Comm.), 1989. **39**(8): p. 5566-5568.*

75. *Abramson, A.R., C.-L. Tien, and A. Majumdar, Interface and strain effects on the thermal conductivity of heterostructures: A molecular dynamics study. Journal of Heat Transfer, 2002. **124**: p. 963-970.*

76. *Picu, R.C., T.B. Tasciuc, and M.C. Pavel, Strain and size effects on heat transport in nanostructures. Journal of Applied Physics, 2003. **93**(6): p. 3535-3539.*

77. *Bhowmick, S. and V.B. Shenoy, Effect of strain on the thermal conductivity of solids. The Journal of Chemical Physics, 2006. **125**.*

78. *Jeng, M.-S., R. Yang, D. Song, and G. Chen, Modeling the thermal conductivity and phonon transport in nanoparticle composites using monte carlo simulation. Journal of Heat Transfer, 2008. **130**(04): p. 022410-1.*

79. *Yang, R., G. Chen, and M.S. Dresselhaus, Thermal conductivity of simple and tubular nanowire composites in the longitudinal direction. Phys. Rev. B, 2005. **72**.*

80. *Huang, X., X. Huai, S. Liang, and X. Wang, Thermal transport in Si/Ge nanocomposites. J. Phys. D: Appl. Phys., 2009. **42**: p. 095416.*

81. *Yang, R. and G. Chen, Thermal conductivity modeling of periodic two-dimensional nanocomposites. Phys. Rev. B, 2004. **69**.*

82. *Volz, S., J.B. Saulnier, G. Chen, and P. Beauchamp, Computation of thermal conductivity of Si/Ge superlattices by molecular dynamics techniques. Microelectronics J., 2000. **31**: p. 815-819.*

83. *Samvedi, V. and V. Tomar, Role of heat flow direction, monolayer film thickness, and periodicity in controlling thermal conductivity of a Si-Ge superlattice system. Journal of Applied Physics, 2009. **105**.*